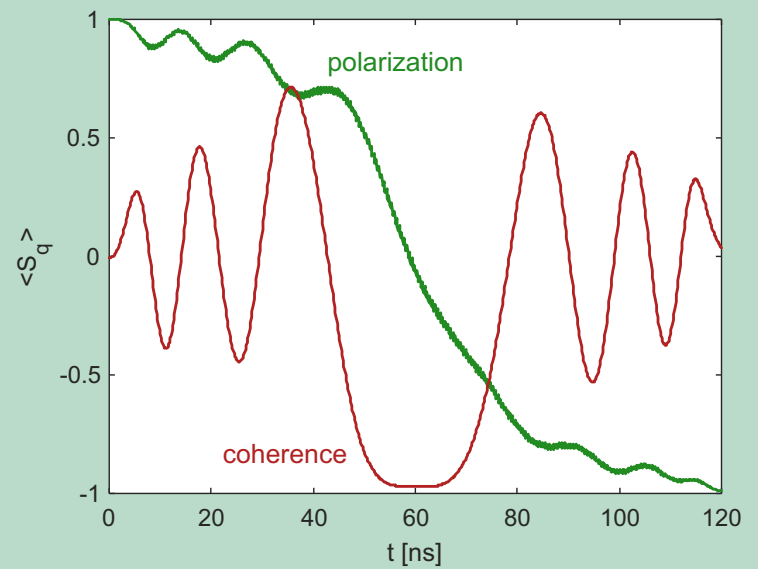
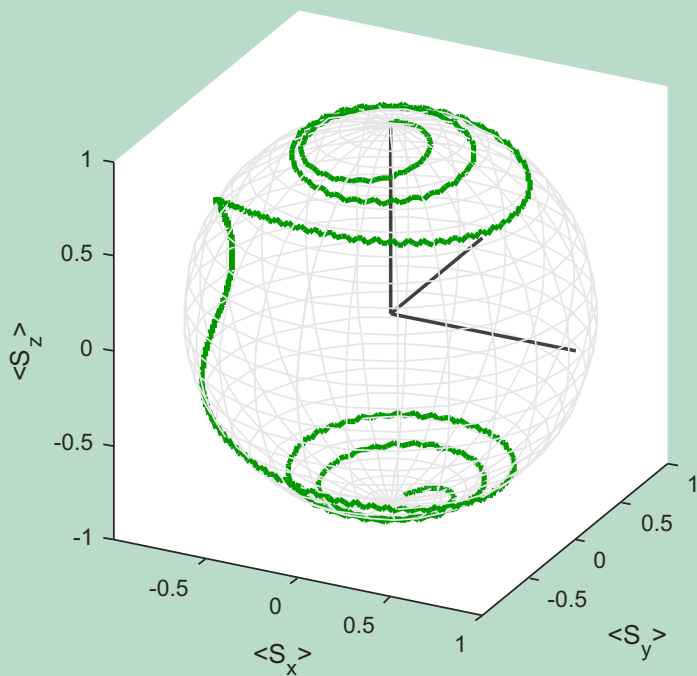


# Advanced Magnetic Resonance

Spin Dynamics Computations and Phenomena in Hyperfine-Coupled Systems

Gunnar Jeschke



Copyright © 2021 Gunnar Jeschke

PUBLISHED BY GUNNAR JESCHKE, ETH ZÜRICH

The title page shows a simulation of the effect of a linearly frequency-swept pulse on a transition passed at half the pulse length.

*First printing, September 2021*

# Contents

<b>1</b>	<b>Introduction</b>	<b>7</b>
<b>1.1</b>	<b>Topics and Organization of the Lecture Course</b>	<b>7</b>
1.1.1	Prerequisites . . . . .	7
1.1.2	Topics . . . . .	7
<b>1.2</b>	<b>Literature &amp; Software</b>	<b>8</b>
<b>1</b>	<b>Spin Dynamics Computations</b>	
<b>2</b>	<b>Basics of Spin Dynamics Computations</b>	<b>11</b>
<b>2.1</b>	<b>Spin Operators</b>	<b>11</b>
2.1.1	Spin Wavefunction . . . . .	11
2.1.2	Pauli Matrices . . . . .	12
2.1.3	Spin Ensembles in a Mixed State - The Density Operator . . . . .	12
2.1.4	Systems with Coupled Spins . . . . .	14
2.1.5	Spin Hamiltonian . . . . .	15
<b>2.2</b>	<b>Equations of Motion</b>	<b>16</b>
2.2.1	Liouville-von-Neumann Equation . . . . .	16
2.2.2	Superoperators and the Stochastic Liouville Equation . . . . .	17
<b>2.3</b>	<b>Thermal Equilibrium</b>	<b>18</b>
2.3.1	High-temperature Approximation . . . . .	18
2.3.2	Quantum Symmetries . . . . .	19
<b>3</b>	<b>Passage Effects</b>	<b>21</b>
<b>3.1</b>	<b>Excitation and Detection</b>	<b>21</b>
3.1.1	Classical Description of the Excitation Field . . . . .	21

3.1.2	Bloch-Siegert Shift	23
3.1.3	Arbitrary Waveform Excitation and Frequency Sweeps	24
3.1.4	Bandwidth Limitations and Deadtime	25
<b>3.2</b>	<b>Passage of a Single Transition</b>	<b>26</b>
3.2.1	Linear Frequency Sweep with Constant Amplitude	26
3.2.2	Adiabaticity and Flip Angle upon Passage	27
3.2.3	Offset-independent Adiabaticity	28
3.2.4	Phase Dispersion and Echo Refocusing	30
3.2.5	Resonator Compensation	32
<b>3.3</b>	<b>Passage in Multi-level Systems</b>	<b>33</b>
3.3.1	Sequential Single-passage Approximation	33
3.3.2	Longitudinal Interference	33
3.3.3	Transverse Interference	34
3.3.4	Multi-photon Transitions	35
<b>4</b>	<b>Hole Burning and Shifting</b>	<b>37</b>
<b>4.1</b>	<b>Inhomogeneous Line and Selective Inversion</b>	<b>37</b>
4.1.1	Width and Shape of the Spectral Hole	38
4.1.2	Spectral Grating	39
<b>4.2</b>	<b>Hole Burning in Multi-Level Systems</b>	<b>40</b>
4.2.1	Enhanced Hole Burning for Weakly Allowed Transitions	40
4.2.2	Side Holes	41
4.2.3	ELDOR-detected NMR	42
4.2.4	Solid-effect DNP	43
<b>4.3</b>	<b>Hole Shifting</b>	<b>43</b>
4.3.1	Non-selective Hole Shifting	43
4.3.2	Selective Hole Shifting	44
4.3.3	Shifting a Spectral Grating	45

## II

## Controlling Hyperfine Interaction

<b>5</b>	<b>Hyperfine Decoupling</b>	<b>49</b>
<b>5.1</b>	<b>Secular Hyperfine Interaction</b>	<b>49</b>
<b>5.2</b>	<b>Effect of the Pseudosecular Hyperfine Interaction</b>	<b>52</b>
<b>6</b>	<b>Dynamical Decoupling</b>	<b>55</b>
<b>6.1</b>	<b>Phenomenological Aspects of Dynamical Decoupling</b>	<b>55</b>
<b>6.2</b>	<b>Cluster Correlation Expansion</b>	<b>56</b>
<b>6.3</b>	<b>Three-spin Model of Dynamical Decoupling</b>	<b>57</b>
6.3.1	Defining a Minimal System	57
6.3.2	Product Operator Formalism for the Refocusing Block	57
	<b>Bibliography</b>	<b>61</b>
	<b>Books</b>	<b>61</b>
	<b>Articles</b>	<b>61</b>





# 1. Introduction

## 1.1 Topics and Organization of the Lecture Course

### 1.1.1 Prerequisites

This lecture course presupposes a basic knowledge of magnetic resonance, including description by spin Hamiltonians and their expression in terms of Pauli matrices. At ETH Zurich, these topics are covered in the lecture course PC IV - Magnetic Resonance. A good textbook for closing gaps is Malcolm Levitt's "Spin Dynamics" [Lev08]. Somewhat more "old school", but also fully adequate for this purpose, is the book on pulse EPR by Arthur Schweiger and the author of these lecture notes [SJ01]. Both these books also cover density operator and product operator formalism, which we use in this lecture course and introduce only briefly.

### 1.1.2 Topics

These lecture notes cover the first part of a combined course on electron paramagnetic resonance (EPR) spectroscopy and dynamic nuclear polarization (DNP). Thus, our main interest is in electron-nuclear spin systems. We consider the measurement of nuclear spin frequencies by detection of electron spins, transfer of polarization from electron to nuclear spins, and the decoupling of the hyperfine interaction for increasing resolution of EPR or NMR experiments. Finally, we also treat the special case where tunnel states of methyl groups couple to nuclear and electron spins. To these ends, we first discuss the computational description of spin dynamics via density operator formalism (Chapter 2). Going beyond standard textbook treatments, we consider excitation of the spin system by arbitrary waveforms, as it is nowadays feasible in both NMR and EPR spectroscopy. In this context, and as a preparation for the DNP part of the lecture course, we briefly touch instrumental aspects of excitation and detection.

Many aspects of arbitrary waveform excitation can be understood in terms of sweeps of the excitation frequency. Such sweeps lead to adiabatic or fast passage of transitions and to interference effects upon subsequent passage of two transitions that share a level (Chapter 3). Another interesting aspect is the selective excitation of spin packets in an


inhomogeneously broadened line. Such excitation leads to hole burning and subsequent excitation of connected transitions leads to frequency shifts of the hole. If two transitions that share a level are both at least weakly allowed, burning a hole on one of these transitions creates a side hole on the other transition. This effect underlies solid-effect DNP and electron electron double resonance (ELDOR) detected NMR. Phenomena related to hole burning and hole shifting are discussed in Chapter 4, which concludes the block on general description of spin dynamics.

The second block is devoted to control of the hyperfine interaction. In Chapter 5 we treat hyperfine decoupling, which differs from typical decoupling schemes in NMR because of the large ratio between the gyromagnetic ratios of electron and nuclear spins. Therefore, irradiation of electron spins is much more efficient for decoupling, even in situations where the final detection is again on the electron spin. The situation, where an electron spin is weakly coupled to a large bath of nuclear spins, which are in turn coupled among themselves, is of special interest for both DNP and pulsed EPR. In DNP, the weak hyperfine coupling is used for transferring polarization from the electron spin to nuclear spins, whereas the couplings between nuclear spins cause spin diffusion and thus redistribution of this polarization among the nuclei. Such nuclear spin diffusion also leads to coherence loss of the electron spins (short: decoherence). This decoherence can be partially suppressed by dynamical decoupling, which we discuss in Chapter 6.

## 1.2 Literature & Software

As an advanced course, this series of lectures contains much material which is not covered by textbooks. However, most of the formalism for describing spin dynamics is very well explained by Levitt's book [Lev08]. Where necessary, we will complement references to this book by references to reviews or even original research articles. Many of the concepts are easier to understand by actually running spin dynamics simulations and analyzing their results. Our toolbox SPIn DYnamics ANalysis (SPIDYAN) [PDJ16] is integrated into the development version of the popular [EasySpin](#) package [SS06] for simulation of EPR spectra and experiments. Our examples were tested with [version 6.0.0-dev.33](#), which comes as a compiled Matlab toolbox. It is instructive to view the source code, which is [available at GitHub](#). Where appropriate, we will refer to this source code.

References lists for sections have the form

 [Lev08]:11.1; [SJ01]4.2.2; `sop`

meaning that the concepts are treated in more detail in sections 11.1 and 4.2.2 of the books by Levitt and Schweiger/Jeschke, respectively and that the source code of EasySpin function `sop` is instructive for understanding computational implementation.



# Spin Dynamics Computations

<b>2</b>	<b>Basics of Spin Dynamics Computations</b>	<b>11</b>
2.1	Spin Operators	
2.2	Equations of Motion	
2.3	Thermal Equilibrium	
<b>3</b>	<b>Passage Effects</b>	<b>21</b>
3.1	Excitation and Detection	
3.2	Passage of a Single Transition	
3.3	Passage in Multi-level Systems	
<b>4</b>	<b>Hole Burning and Shifting</b>	<b>37</b>
4.1	Inhomogeneous Line and Selective Inversion	
4.2	Hole Burning in Multi-Level Systems	
4.3	Hole Shifting	



```
In[59]:= TEB = 2 eta (S[1, z] × S[2, y] × S[3, x] - S[1, z] × S[2, x] × S[3, y])
```

```
Out[59]= 2 eta (S1,z S2,y S3,x - S1,z S2,x S3,y)
```

```
In[60]:= rho0 = S[1, x]
```

```
Out[60]= S1,x
```

```
In[61]:= rho0EB = app[rho0, TEB]
```

```
Out[61]= Cos[ $\frac{\text{eta}}{2}$ ]2 S1,x + 4 Cos[ $\frac{\text{eta}}{2}$ ] S1,y S2,y S3,x Sin[ $\frac{\text{eta}}{2}$ ] - 4 Cos[ $\frac{\text{eta}}{2}$ ] S1,y S2,x S3,y Sin[ $\frac{\text{eta}}{2}$ ] + 4 S1,x S2,z S3,z Sin[ $\frac{\text{eta}}{2}$ ]2
```



# EasySpin

## 2. Basics of Spin Dynamics Computations

*This Chapter starts with a brief repetition of the basic mathematical concepts for computing transition frequencies, transition moments, and time evolution of a quantum ensemble in a mixed state. We then relate the spin operator treatment to the physics and instrumentation for excitation and detection of spins. On this basis, we discuss excitation by arbitrary waveforms, digital filtering, and digital downconversion. The Chapter concludes with a brief treatment of the system consisting of an electron spin  $S = 1/2$  and a nuclear spin  $I = 1/2$ . This system serves as a basis for discussing multi-level systems in the following Chapters.*

### 2.1 Spin Operators

#### 2.1.1 Spin Wavefunction

Usually, spins couple so weakly to their environment that magnetic resonance experiments can be well approximated in a spin-only quantum subspace. Except for Chapter ??, we shall consider only quantum subspaces that arise from coupled electron spins  $S_j$  and nuclear spins  $I_k$ . Most of the time, we will restrict ourselves to spins of one unpaired electron ( $S_j = 1/2$ ) and of nuclei with spin quantum number  $I_k = 1/2$ . A spin  $S = 1/2$  has two eigenstates  $|\alpha\rangle$  and  $|\beta\rangle$ . Hence, its wavefunction is generally given by

$$|\psi\rangle = c_\alpha |\alpha\rangle + c_\beta |\beta\rangle . \quad (2.1)$$

The two coefficients  $c_\alpha$  and  $c_\beta$  are complex and we can normalize the wavefunction

$$|c_\alpha|^2 + |c_\beta|^2 = 1 . \quad (2.2)$$

As usual, absolute phase of the wavefunction is not experimentally accessible. However, unless the spin is in an eigenstate ( $c_\alpha = 1, c_\beta = 0$  or  $c_\alpha = 0, c_\beta = 1$ ), there is a relative phase of the superposition of the two eigenstates. Each of the complex coefficients has phase  $\phi_i = \arctan[\Im(c_i), \Re(c_i)]^1$  and phase  $\phi = \phi_\alpha - \phi_\beta$  is, in principle, observable.

<sup>1</sup>The arc tangent with the two arguments imaginary and real part of  $c_i$  has a codomain of width  $2\pi$ .

### 2.1.2 Pauli Matrices

If we define a Cartesian frame, we can perform three possible measurements on the spin, providing components along  $x$ ,  $y$ , and  $z$ . The three observables correspond to operators  $\hat{S}_x$ ,  $\hat{S}_y$ , and  $\hat{S}_z$ . Let us consider a wavefunction with  $c_\alpha = 1/\sqrt{2}$  and  $c_\beta = -1/\sqrt{2}$ . The expectation value of  $\hat{S}_x$  is given by

$$\langle \hat{S}_x \rangle = \langle \psi | \hat{S}_x | \psi \rangle . \quad (2.3)$$

We can express the wavefunction bra by a two-element row vector, the spin operator by a  $2 \times 2$  matrix, and the wavefunction ket by a two-element column vector

$$\langle \hat{S}_x \rangle = (c_\alpha \quad c_\beta) \begin{pmatrix} 0 & 1/2 \\ 1/2 & 0 \end{pmatrix} \begin{pmatrix} c_\alpha \\ c_\beta \end{pmatrix} . \quad (2.4)$$

where the  $2 \times 2$  matrix is the *Pauli matrix* for  $\hat{S}_x$ . We easily ascertain  $\langle \hat{S}_x \rangle = -1$  for the case at hand. The other two Pauli matrices are


$$\hat{S}_y = \begin{pmatrix} 0 & -i/2 \\ i/2 & 0 \end{pmatrix} \quad (2.5)$$

and

$$\hat{S}_z = \begin{pmatrix} 1/2 & 0 \\ 0 & -1/2 \end{pmatrix} . \quad (2.6)$$

For our wavefunction, they both have expectation values of 0.

The electron group spin  $S > 1/2$  of a high-spin species has  $2S+1$  eigenstates; this applies in analogy to quadrupole nuclei. It follows that their wavefunctions must be represented by vectors with  $2S+1$  elements and their spin operators by  $(2S+1) \times (2S+1)$  matrices. Details can be found in the following literature and source code:

 [Lev08]:7.9; [SJ01]:B.2.2; `sop`

**EasySpin example 2.1.1** — Verify that the commutator of  $\hat{S}_x$  and  $\hat{S}_y$  is  $i\hat{S}_z$ .

```
Sx = sop(1/2, 'x');
Sy = sop(1/2, 'y');
Sz = sop(1/2, 'z');
commutator = Sx*Sy - Sy*Sx;
disp(max(max(commutator - 1i*Sz)));
```

### 2.1.3 Spin Ensembles in a Mixed State - The Density Operator

We now consider a large ensemble of spins of the same type as we need it to describe a magnetic resonance experiment on a macroscopic sample. What we did in the previous section will still work, if and only if all spins have the same wavefunction. Such a state of the ensemble is called *pure state*. This is very hard to achieve because energies of spin interactions are so small. Therefore, we usually cannot reach temperatures where all spin (systems) are in their ground state before the start of the experiment. The ensemble is in a *mixed state* from the very beginning and will remain in a mixed state upon excitation.

The mixed state can no longer be characterized by a vector with  $2S + 1$  components. Instead of averaging the ket and bra separately, which would destroy normalization, we can take the ensemble average over their outer product to obtain the *density operator*  $\hat{\rho}$

$$\hat{\rho} = \sum_i |\psi_i\rangle\langle\psi_i|. \quad (2.7)$$

Because of the mathematical relationship between the ket and bra vectors,  $\hat{\rho}$  must be represented by a Hermitian density matrix

$$\hat{\rho} = \begin{pmatrix} \overline{|c_\alpha|^2} & \overline{c_\alpha c_\beta^*} \\ c_\alpha^* c_\beta & |c_\beta|^2 \end{pmatrix}, \quad (2.8)$$

where the overbar denotes the ensemble average and the asterisk the complex conjugate. We can generally express the two off-diagonal elements for spin  $1/2$  by a linear combination of  $\hat{S}_x$  and  $\hat{S}_y$ , since the lower off-diagonal element is the complex conjugate of the upper one. However, we cannot generally write the diagonal elements as a multiple of  $\hat{S}_z$ . Therefore, we need to complete our operator basis by the unit operator

$$\hat{\mathbb{1}} = \begin{pmatrix} 1 & 0 \\ 0 & 1 \end{pmatrix}. \quad (2.9)$$

For spins higher than  $1/2$ , products and powers of the Cartesian spin operators are required for expressing the density operator by a linear combination of spin operators.

**EasySpin example 2.1.2** — Compute the matrix representation of  $\hat{S}_x^2 - \hat{S}_y^2$  for spin  $S = 1$ .

```
Sx = sop(1, 'x');
Sy = sop(1, 'y');
disp(Sx^2 - Sy^2);
```

The density operator contains the full information on an ensemble that is experimentally accessible. Any observable can be associated with an operator  $\hat{O}$  and its expectation value is computed by

$$\langle\hat{O}\rangle = \text{Tr}\{\hat{O}\hat{\rho}\}. \quad (2.10)$$

This equation applies to Hermitian operators. The ladder operator  $\hat{S}^+ = \hat{S}_x + i\hat{S}_y$  used to model quadrature detection is not Hermitian.

**EasySpin example 2.1.3** — Compute the "expectation value" of  $\hat{S}^-$ .

```
Sp = sop(1/2, '+'); % this generates S^+
Sm = sop(1/2, '-'); % this generates S^-
rho = sop(1/2, 'x') + 1i*sop(1/2, 'y'); % this sets the density
operator to S^-
detected1 = trace(Sp*rho);
detected2 = trace(Sm*rho);
fprintf(1, 'Density operator artificially set to S^+\n');
fprintf(1, 'Computed with S^+: %6.3f\n', detected1);
fprintf(1, 'Computed with S^-: %6.3f\n', detected2);
```

### 2.1.4 Systems with Coupled Spins

For computational efficiency, we define the spin system as small as possible. Where the border can be drawn depends on the total time  $t_{\max}$  of the observation and the couplings  $c_{j,k}$  in pairs  $(S_j, S_k)$  of spins. If we observe or excite spin  $S_j$ , we must include spin  $S_k$  unless  $c_{j,k}t_{\max} \ll 1$ . The coupling is expressed as an angular frequency. This consideration propagates: For every spin that we have already included, we need to apply the same reasoning to all its coupling partners that we have not yet included. Sometimes, this makes the problem intractable. In this case, spins that are remote from the spin of interest but that still contribute on the time scale of the experiment are treated collectively as a *spin bath*.

For the spins that are treated explicitly, each state of each spin can be combined with each state of each other spin. In other words, the total number of states in a system with  $E$  electron spins  $S_j$  and  $N$  nuclear spins  $I_k$  is given by

$$n_{\text{Hilbert}} = \prod_{j=1}^E (2S_j + 1) \prod_{k=1}^N (2I_k + 1). \quad (2.11)$$

This exponential growth of the Hilbert space dimension  $n_{\text{Hilbert}}$  for a linear increase in the number of explicitly treated spins is a major problem for computational spin dynamics, especially in the solid state.

Since state space is the outer product of the subspaces, matrix representations of the required product operators can also be expressed as outer products (Kronecker products) of the subspace operators. For example, the product operator  $\hat{S}_z \hat{I}_x$  in a system  $S = 1/2$ ,  $I = 1/2$  is given by

$$\hat{S}_z \hat{I}_x = \begin{pmatrix} 1/2 & 0 \\ 0 & -1/2 \end{pmatrix} \otimes \begin{pmatrix} 0 & 1/2 \\ 1/2 & 0 \end{pmatrix} = \begin{pmatrix} 0 & 1/4 & 0 & 0 \\ 1/4 & 0 & 0 & 0 \\ 0 & 0 & 0 & -1/4 \\ 0 & 0 & -1/4 & 0 \end{pmatrix}. \quad (2.12)$$

Matrix representations of single-spin operators are computed as outer products with the identity operators of all other spins in the proper sequence. For example,

$$\hat{S}_z = \begin{pmatrix} 1/2 & 0 \\ 0 & -1/2 \end{pmatrix} \otimes \begin{pmatrix} 1 & 0 \\ 0 & 1 \end{pmatrix} = \begin{pmatrix} 1/2 & 0 & 0 & 0 \\ 0 & 1/2 & 0 & 0 \\ 0 & 0 & -1/2 & 0 \\ 0 & 0 & 0 & -1/2 \end{pmatrix} \quad (2.13)$$

and

$$\hat{I}_z = \begin{pmatrix} 1 & 0 \\ 0 & 1 \end{pmatrix} \otimes \begin{pmatrix} 1/2 & 0 \\ 0 & -1/2 \end{pmatrix} = \begin{pmatrix} 1/2 & 0 & 0 & 0 \\ 0 & -1/2 & 0 & 0 \\ 0 & 0 & 1/2 & 0 \\ 0 & 0 & 0 & -1/2 \end{pmatrix}. \quad (2.14)$$

**EasySpin example 2.1.4 — Construction of operators for a system  $S = 1/2$ ,  $I = 1/2$ .**

```
Sz = sop([1/2 1/2], 'ze');
Iz = sop([1/2 1/2], 'ez');
SzIz = sop([1/2 1/2], 'zz');
```

$$\text{SzIx} = \text{sop}([1/2, 1/2], 'zx');$$

### 2.1.5 Spin Hamiltonian

The spin subspace of a large quantum system has its own Hamiltonian  $\hat{\mathcal{H}}_{\text{spin}}$  that can be derived by projecting the total Hamiltonian to this subspace. We need this spin Hamiltonian in order to compute the time evolution of the spin wavefunction by the time-dependent Schrödinger equation

$$i \frac{\partial}{\partial t} \psi = \hat{\mathcal{H}}_{\text{spin}} \psi . \quad (2.15)$$

For simplicity, we have expressed the spin Hamiltonian in angular frequency units. In general,  $\hat{\mathcal{H}}_{\text{spin}}$  is time-dependent. This time dependence arises from spatial reorientation of the spin system in an external magnetic field, electromagnetic fields used by the experimenter for excitation, and environmental fluctuations that cause fluctuating magnetic fields at the spins. We express this Hamiltonian by a sum of three terms

$$\hat{\mathcal{H}}_{\text{spin}} = \hat{\mathcal{H}}_0 + \hat{\mathcal{H}}_1 + \hat{\mathcal{H}}_2 . \quad (2.16)$$

The term  $\hat{\mathcal{H}}_0$  is the time-independent part, except that we may include into it macroscopic sample reorientation imposed by the experimenter, such as magic-angle sample spinning in solid-state NMR. In this part of the lecture course, we consider only experiments without such macroscopic sample reorientation. The term  $\hat{\mathcal{H}}_1$  describes excitation by electromagnetic fields and is deterministically time-dependent in the laboratory frame. Sometimes, the time-dependence can be removed by imposing a time-dependent frame transformation, such as going to the rotating frame for irradiation with a fixed frequency. In general, this is called an *interaction frame* transformation. The term  $\hat{\mathcal{H}}_2$  is stochastically time-dependent due to stochastic reorientation of the spin system or fluctuations in the environment of the spin system. It is either neglected or treated by relaxation theory. The reorientation component can be neglected in the fast motion limit, where instead an isotropic orientation average of  $\hat{\mathcal{H}}_0$  can be used. Spin relaxation is usually dominated by  $\hat{\mathcal{H}}_2$ . It is not always possible to model  $\hat{\mathcal{H}}_2$  or to predict the relaxation times even if a plausible mechanism is known. In such cases the effect of  $\hat{\mathcal{H}}_2$  is accounted for by empirical relaxation times, which can be experimentally determined. One often assumes exponential relaxation decay, but as we shall see later, this is not always a good approximation.

Each Hamiltonian term on the right-hand side of Eq. (2.16) can be expressed in the following form

$$\hat{\mathcal{H}}_i = \sum_j (\omega_{j,x} \quad \omega_{j,y} \quad \omega_{j,z}) \begin{pmatrix} \hat{S}_{j,x} \\ \hat{S}_{j,y} \\ \hat{S}_{j,z} \end{pmatrix} + \sum_j \sum_k (\hat{S}_{j,x} \quad \hat{S}_{j,y} \quad \hat{S}_{j,z}) \mathbf{C}_{j,k} \begin{pmatrix} \hat{S}_{k,x} \\ \hat{S}_{k,y} \\ \hat{S}_{k,z} \end{pmatrix} , \quad (2.17)$$

where the  $\omega_{j,\xi}$  are in general time dependent and the  $\mathbf{C}_{j,k}$  are  $3 \times 3$  interaction matrices that describe spin-spin couplings, which can also be time dependent. Terms with  $j = k$  in the double sum exist only for spins  $S_j > 1/2$ .

As an example, we consider the static Hamiltonian  $\hat{\mathcal{H}}_0$  for the system of an electron spin  $S = 1/2$  and a nuclear spin  $I = 1/2$  with secular hyperfine coupling  $A$ , pseudo-secular hyperfine coupling  $B$ , nuclear Zeeman frequency  $\omega_I$ , and electron Zeeman frequency  $\omega_S$ .

$$\hat{\mathcal{H}}_0 = \omega_S \hat{S}_z + \omega_I \hat{I}_z + A \hat{S}_z \hat{I}_z + B \hat{S}_z \hat{I}_x . \quad (2.18)$$

We have defined the required product operators for EasySpin computations in example 2.1.4. If we decide on units of Megahertz and microseconds for frequency and time, we can construct the Hamiltonian as follows.

**EasySpin example 2.1.5 — Spin Hamiltonian for a system  $S = 1/2, I = 1/2$ .**

```

mw_freq = 9500; % 9.5 GHz = 9500 MHz
wS = 2*pi*9500; % angular frequency
B0 = wS*1e6/(gfree*bmagn*hbar); % compute static field in T
gH = nucgval('1H'); % nuclear g value for proton
wI = -gH*nmagn*hbar*B0/1e6; % proton nuclear Zeeman frequency
A = 2*pi*6.3; % moderately coupled proton
B = 2*pi*3.7;
H0 = wS*Sz + wI*Iz + A*SzIz + B*SzIx;

```

**2.2 Equations of Motion****2.2.1 Liouville-von-Neumann Equation**

By applying the time-dependent Schrödinger equation to both the wavefunction ket and bra and inserting the results into Eq. (2.7), one can derive the Liouville-von-Neumann equation for the evolution of the density operator

$$\frac{\partial}{\partial t} \hat{\rho} = -i[\hat{H}_{\text{spin}}, \hat{\rho}]. \quad (2.19)$$

This equation of motion can be formally integrated for time intervals where  $\hat{H}_{\text{spin}}$  is time-independent. If time dependence cannot be removed, such formal integration can still be used for sufficiently short time intervals  $\Delta t$ . We obtain

$$\hat{\rho}(t + \Delta t) = \exp(-i\hat{H}_{\text{spin}}\Delta t)\hat{\rho}(t)\exp(i\hat{H}_{\text{spin}}\Delta t) = \hat{U}\hat{\rho}(t)\hat{U}^\dagger, \quad (2.20)$$

where  $\hat{U}$  is called a propagator and  $\hat{U}^\dagger$  is its adjoint, the latter being much more efficient to compute than a matrix exponential.

As an example, we consider evolution of electron coherence that has initial phase  $x$  under the spin Hamiltonian defined in examples 2.3.1 and 2.1.4. We apply the rotating-wave approximation and add a resonance offset of 2 MHz in order to mimic heterodyne detection.

**EasySpin example 2.2.1 — Evolution of electron coherence under hyperfine coupling.**

```

det = sop([1/2 1/2], '-e'); % detection operator
rho = sop([1/2 1/2], 'xe'); % electron spin coherence in phase
H0_RWA = H0 - wS*Sz; % rotating-wave approximation
H0_RWA = H0_RWA + 2*pi*2*Sz; % 2 MHz resonance offset
dt = 0.010; % time increment 10 ns
ndat = 1024; % number of data points
data = zeros(1, ndat); % complex data vector
t = 0:dt:(ndat-1)*dt; % time axis (microseconds)
U = expm(-1i*H0_RWA*dt); % propagator
for k = 1:ndat % detection loop
    data(k) = trace(det*rho); % detection
    rho = U*rho*U'; % time evolution for time dt
end
figure(1); clf; hold; % prepare plot
plot(t, real(data));
plot(t, imag(data));

```



```
xlabel('time (\mus)');
```

Note the use of the matrix exponential function `expm` in computing the propagator. Application of the elementwise exponential function `exp` leads to wrong results.

 [SJ01]:4.2.1

### 2.2.2 Superoperators and the Stochastic Liouville Equation

The Liouville-von-Neumann equation conserves entropy and cannot describe relaxation. Thus, it corresponds to complete neglect of the environment term  $\hat{\mathcal{H}}_2$  in Eq. (2.16). In general, relaxation can effect transfers from any element of the density matrix to any other element. This is described by a relaxation superoperator  $\hat{\Gamma}$ . The effect of a superoperator  $\hat{O}$  on the density operator is computed by

$$\left(\hat{O}\hat{\rho}\right)_{kl} = \sum_m \sum_n O_{klmn} \rho_{mn} . \quad (2.21)$$

We see that, while an matrix elements of an operator correspond to a pair of states in Hilbert space, matrix elements of the superoperator correspond to pairs of state pairs. The space of Hilbert space pairs is called *Liouville space*. The Liouville space dimension is thus the square of the Hilbert space dimension  $n_{\text{Hilbert}}$ . Instead of using two-dimensional arrays (matrices) for operators and four-dimensional arrays for superoperators, it is more convenient to reshape the operators to a vector, which corresponds to reshaping the superoperators to a matrix.

The equation of motion including relaxation is the stochastic Liouville equation

$$\frac{\partial}{\partial t} \hat{\rho} = -i\hat{\mathcal{H}}\hat{\rho} - \hat{\Gamma}(\hat{\rho} - \hat{\rho}_{\text{ss}}) , \quad (2.22)$$

where

$$\hat{\mathcal{H}}_{klmn} = \hat{\mathcal{H}}_{km} \delta_{nl} - \delta_{km} \hat{\mathcal{H}}_{nl} \quad (2.23)$$

is the Hamiltonian superoperator with the Kronecker deltas  $\delta_{nl}$  and  $\delta_{km}$  and  $\hat{\mathcal{H}} = \hat{\mathcal{H}}_0 + \hat{\mathcal{H}}_1$ ,  $\hat{\mathcal{H}}_2$  having been replaced by  $\hat{\Gamma}$ . The steady-state density operator  $\hat{\rho}_{\text{ss}}$  is often approximated by the thermal equilibrium density operator  $\hat{\rho}_{\text{eq}}$  introduced in Section 2.3. This approximation is good only in the limit of weak irradiation where the experimental steady state is not significantly perturbed from the equilibrium state. It follows that this approximation should not be used during strong irradiation. The steady-state solution depends on irradiation, i.e., on  $\hat{\mathcal{H}}_1$ , and is thus best computed for each time interval where  $\hat{\mathcal{H}}_1$  can be considered as constant. By setting the left-hand side of the stochastic Liouville equation zero and replacing on the right-hand side  $\hat{\rho}_{\text{ss}}$  by  $\hat{\rho}_{\text{eq}}$  and  $\hat{\rho}$  by  $\hat{\rho}_{\text{ss}}$ , we find the approximation

$$\hat{\rho}_{\text{ss}} = \left(i\hat{\mathcal{H}} + \hat{\Gamma}\right)^{-1} \hat{\Gamma} \hat{\rho}_{\text{eq}} . \quad (2.24)$$

It has been argued that this approximation is problematic because the *Liouvillian*


$$\hat{\mathcal{L}} = i\hat{\mathcal{H}} + \hat{\Gamma} \quad (2.25)$$

is singular due to conservation of the total number of spins [RSB91]. The problem can be solved by introducing invariance of the trace of  $\hat{\rho}$  in the equation. With  $\hat{\rho}_{\text{ss}}$  being known, the stochastic Liouville equation can be formally integrated, giving

$$\hat{\rho}(t + \Delta t) = \hat{\rho}_{\text{ss}} + (\hat{\rho}(t) - \hat{\rho}_{\text{ss}}) \exp(\hat{\mathcal{L}}\Delta t) . \quad (2.26)$$

The function `spidy` of EasySpin treats relaxation by implementing Eqs. (2.24) and (2.26) in its subfunction `s_thyme`.

The most general equation of motion for open quantum systems is the Lindblad equation. We do not further discuss the Lindblad equation, since the stochastic Liouville equation suffices for our purposes.

 [Pri18]2.3.3; `s_thyme`

## 2.3 Thermal Equilibrium

Most magnetic resonance experiments start from the thermal equilibrium state of the spin system. For predicting the outcome, we thus need to know the thermal equilibrium density operator  $\hat{\rho}_{\text{eq}}$ . Further, we need to know  $\hat{\rho}_{\text{eq}}$  in order to compute the steady-state density operator for application of the stochastic Liouville equation according to Eq. (2.24).

Because of the small interaction energies in spin systems, quantum symmetry restrictions can usually be disregarded and  $\hat{\rho}_{\text{eq}}$  can be computed to a very good approximation by Maxwell-Boltzmann statistics,

$$\hat{\rho}_{\text{eq}} = \frac{e^{-\hbar\hat{\mathcal{H}}/k_{\text{B}}T}}{\text{Tr}\left\{e^{-\hbar\hat{\mathcal{H}}/k_{\text{B}}T}\right\}} , \quad (2.27)$$

where  $k_{\text{B}}$  is the Boltzmann constant and  $T$  the sample temperature. The laboratory-frame Hamiltonian must be used.

### 2.3.1 High-temperature Approximation

In the *high-temperature approximation*, where the difference between the largest and smallest eigenvalue of  $\hat{\mathcal{H}}$  is much smaller than the thermal energy  $k_{\text{B}}T$ , we can approximate  $e^{-x} = 1 - x$  and obtain

$$\hat{\rho}_{\text{eq}} \approx \hat{\mathbb{1}} - \frac{\hbar\hat{\mathcal{H}}}{k_{\text{B}}T} . \quad (2.28)$$

This approximation is very useful for analytical computations. Within the high-field approximation for spins  $1/2$ , it suffices to consider the Zeeman terms of  $\hat{\mathcal{H}}$ . If an electron spin is present, the nuclear Zeeman terms can usually be dropped as well. For spins  $> 1/2$ , it may be necessary to include the nuclear quadrupole or zero-field interactions, especially if heavier elements than second-row elements are involved. For numerical computations, the high-temperature and high-field approximations are unnecessary for computing  $\hat{\rho}_{\text{eq}}$ . We discourage their use and recommend Eq.(2.27) instead.

The high-temperature approximation is usually good for systems consisting of only nuclear spins at all accessible fields and at temperatures down to 1 K. It may be violated in the mK regime. For electron spin  $1/2$ , the high-temperature approximation can easily be violated. The Zeeman energy of an electron spin with  $g \approx 2$  matches the thermal energy at about 4.2 K and 3.35 T, corresponding to a W-band microwave frequency of about 94 GHz.

The following example shows that it may be violated for Gd(III)-based polarizing agents for DNP already at a temperature of 110 K with high-field NMR spectrometers. Polarization of the six allowed transitions in this  $S = 7/2$  system differs strongly under these conditions.

#### EasySpin example 2.3.1 — High-temperature approximation for Gd(III) complexes.

```
T = 110; % typical temperature for ssDNP
nu_1H = 1.2e9; % 1.2 GHz proton frequency
B0 = planck*nu_1H/(nucgval('1H')*nmagn); % magnetic field [T]
g = 2;
nu_EZ = g*bmagn*B0/planck; % electron Zeeman frequency
sz = sop(7/2, 'z');
ham = 2*pi*nu_EZ*sz;
boltzmann_distr = expm(-hbar*ham/(boltzm*T));
rho_eq = boltzmann_distr/trace(boltzmann_distr);
for k = 1:6
    p = rho_eq(7-k,7-k) - rho_eq(8-k,8-k);
    fprintf(1, 'Polarization of transition %i: %6.3f\n', k, p);
end
```

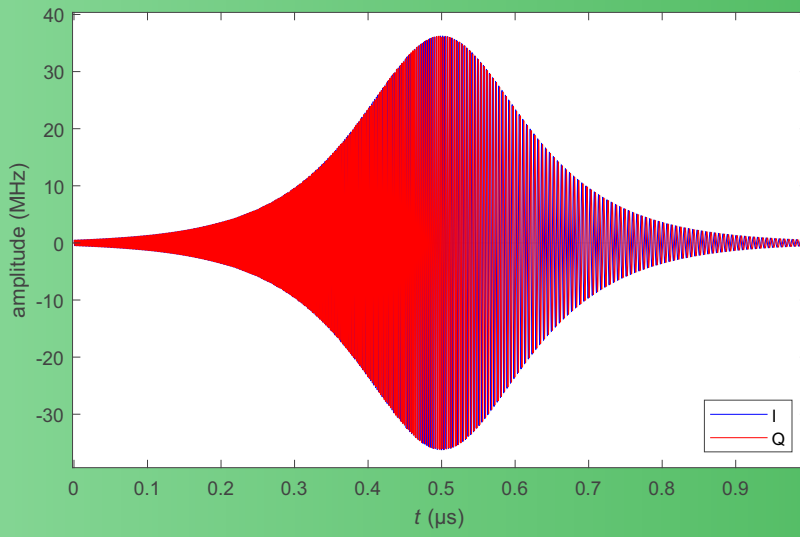
### 2.3.2 Quantum Symmetries

Electrons are Fermions (half-integer spin) and nuclei can be Fermions or Bosons (integer spin). According to the generalized Pauli principle, the total wavefunction must be anti-symmetric with respect to permutation for Fermions and symmetric for Bosons. This may impose restrictions on the symmetry of the spin part of the wavefunction upon exchange of nuclei. Since the electronic wavefunction, electron spin wavefunction, translational wavefunction, and vibrational wavefunction are symmetric with respect to permutation of nuclei, it is the product of the spin part and rotational part of the wavefunction that must fulfil the generalized Pauli principle.

The best known example for such a symmetry restriction is para-hydrogen, which is used for NMR signal enhancement in *para-hydrogen induced polarization* (PHIP). The wavefunction for the rotational ground state ( $J = 0$ ) is symmetric with respect to exchange of the two hydrogen atoms in an  $H_2$  molecule. Accordingly, the spin wavefunction must be antisymmetric in this state, i.e., it must be a singlet wavefunction  $|\alpha_1\beta_2 - \beta_1\alpha_2\rangle/\sqrt{2}$ . While there is no net polarization, the states of the two spins are correlated. This can be seen, for instance, after a hydrogenation reaction that introduces a chemical shift difference between the two protons. The effect is readily observable. At 80 K, where hydrogen is still gaseous, the rotational ground state is much more strongly populated than rotationally excited states.

A similar, but somewhat more involved spin-correlation effect exists for methyl groups with respect to permutation of three protons. This can lead to observable nuclear spin polarization by the *Haupt effect* in solids, provided that the methyl tunnel splitting in the quantum-rotor ground state is much larger than the nuclear Zeeman frequency.





## 3. Passage Effects

*This Chapter starts with a brief treatment of the excitation of spins by an electromagnetic field that is treated classically. We consider resonant irradiation by the rotating-wave approximation and the effect of non-resonant irradiation by computing the Bloch-Siegert shift with Average Hamiltonian Theory. Then we discuss excitation by arbitrary waveforms, in particular by frequency-swept pulses. Such pulses correspond to passage of transitions by the electromagnetic field. We discuss quantitative description of adiabatic passage and define a flip angle for fast passage. Offset-independent adiabaticity (OIA) is introduced as a concept for uniform excitation of spin packets over a wide frequency band. We discuss echo refocusing by OIA pulses, including compensation of dynamic Bloch-Siegert phase. The Chapter concludes with brief explanations of longitudinal and transverse interference effects and of multi-photon excitation. These phenomena occur in spin systems with more than two connected levels.*

### 3.1 Excitation and Detection

#### 3.1.1 Classical Description of the Excitation Field

Spins are excited through their interaction with the magnetic component  $\vec{B}_1(t)$  of an electromagnetic field. If the quantization axis of the spin system is set by an external static magnetic field  $B_0$  and is chosen along  $z$ ,<sup>1</sup>, the excitation Hamiltonian can be written as

$$\hat{\mathcal{H}}_1 = \gamma B_{1,x}(t)\hat{S}_x + \gamma B_{1,y}(t)\hat{S}_y, \quad (3.1)$$

where  $\gamma = g_{\perp}\mu_B/\hbar$  is the gyromagnetic ratio of the electron spin with  $g_{\perp}$  being an effective  $g$  value in the  $xy$  plane that is perpendicular to the static magnetic field. For nuclei,  $g_{\perp}$  is replaced by the negative nuclear  $g$  value  $-g_n$  and the Bohr magneton  $\mu_B$  is replaced by the nuclear magneton  $\mu_n$ .

<sup>1</sup>For strong  $g$  anisotropy, the quantization axis can be tilted with respect to the direction of the external static magnetic field, but we still call it the  $z$  axis.

In order to apply circularly polarized electromagnetic fields one needs to work with cross-coil setups in NMR or special resonators in EPR. This is very rarely done. In most experiments, the field is linearly polarized. We associate the direction of linear polarization with the  $x$  axis of the laboratory frame and redefine  $B_1$  by including a factor of two. The reason for this factor will soon become apparent. Further, we combine sign, gyromagnetic ratio, and time-dependent magnetic field into a field amplitude  $a(t)$  in angular frequency units.

$$\hat{\mathcal{H}}_1 = a(t)\hat{S}_x . \quad (3.2)$$

The simplest case is monochromatic irradiation  $a(t) = 2\omega_1 \cos(\omega_{\text{irr}}t)$ , where  $\omega_{\text{irr}}$  is the frequency of the irradiation field. Such a linearly polarized field at a given frequency can be separated in two circularly polarized components that rotate clockwise (first line on the right-hand side of Eq. (3.3) and anti-clockwise (second line):

$$\begin{aligned} \hat{\mathcal{H}}_1^{(\text{mc})} &= \gamma B_1 \left[ \cos(\omega_{\text{irr}}t)\hat{S}_x + \sin(\omega_{\text{irr}}t)\hat{S}_y \right] + \\ &\quad \gamma B_1 \left[ \cos(\omega_{\text{irr}}t)\hat{S}_x - \sin(\omega_{\text{irr}}t)\hat{S}_y \right] . \end{aligned} \quad (3.3)$$

Magnetization of nuclear spins with positive  $\gamma$  precesses clockwise with Larmor frequency  $\omega_0$ , whereas magnetization of nuclear spins with negative gyromagnetic ratio, as well as of electron spins, precesses anti-clockwise. Without losing generality, we proceed with the electron spin case, which corresponds to  $\omega_0 > 0$ , since the mathematical sense of rotation is anti-clockwise. The component of the excitation field with the same sense of rotation becomes time-independent in a frame that rotates with frequency  $\omega_{\text{irr}}$ . We can transfer to this *rotating frame* by the product operator expression

$$\hat{\mathcal{H}}_1^{(\text{mc})} \xrightarrow{-\omega_{\text{irr}}t\hat{S}_z} \hat{\mathcal{H}}_1 \quad (3.4)$$

and obtain

$$\hat{\mathcal{H}}_1 = \gamma B_1 \hat{S}_x + \gamma B_1 \cos(2\omega_{\text{irr}}t)\hat{S}_x - \gamma B_1 \sin(2\omega_{\text{irr}}t) , \quad (3.5)$$

where the second and third term on the right-hand side correspond to the non-resonant circularly polarized component. For the moment, we drop this component, which corresponds to the *rotating-wave approximation* (RWA). This nicely approximates excitation as long as  $\omega_1 = \gamma B_1 \ll 2\omega_{\text{irr}}$ . Problems can arise in zero-field magnetic resonance or for very small  $g$  values along the static field when  $g_{\perp}$  is large. Even if the RWA is permissible, the component counterrotating with frequency  $2\omega_{\text{irr}}$  causes a Bloch-Siegert shift of the resonance frequency that we will consider in Section 3.1.2.

The rotating-frame transformation is not a transformation between inertial frames. Hence, the static Hamiltonian does not remain invariant. We have

$$\hat{\mathcal{H}}_0^{(\text{RWA})} = \hat{\mathcal{H}}_0 - \omega_{\text{irr}}\hat{S}_z . \quad (3.6)$$

If  $\omega_{\text{irr}}$  changes with time, as we shall consider later on, one can use an accelerating frame. That way the time dependence is shifted from  $\hat{\mathcal{H}}_1$  to  $\hat{\mathcal{H}}_0$ , which can sometimes be convenient.

In the rotating frame, transition frequencies are reduced by the frequency of the irradiation field. Following Cohen-Tannoudji, we can consider this as a dressing of the spin by an irradiation photon. Note that the spin is dressed only as long as the irradiation is switched on. In contrast, we can use the rotating frame also when the irradiation is switched off, i.e., during free evolution and field-free detection. In the case of detection,

the rotating frame corresponds to downconversion of the signal by  $\omega_{\text{irr}}$ , which is usually achieved in magnetic resonance by an IQ mixer. An IQ mixer generates a quadrature signal

$$V(t) = \langle \hat{S}_x^{(\text{RWA})}(t) \rangle + \imath \langle \hat{S}_y^{(\text{RWA})}(t) \rangle . \quad (3.7)$$

Quadrature mixers split the original linearly polarized signal into two components and thus entail some sensitivity loss compared to a simple mixer that detects only  $\hat{S}_x(t)$ . However, if the sign of transition frequencies in the rotating frame is not known *a priori*, use of an IQ mixer for detection is mandatory. This is because a real signal does not carry information on the sign of the frequency.

### 3.1.2 Bloch-Siegert Shift

The counter-rotating circularly polarized component of the linearly polarized irradiation field is non-resonant. We treat the more general case of the effect of non-resonant irradiation by any frequency  $\omega_{\text{nonres}}$  on a spin with Zeeman frequency  $\omega_{\text{Zeeman}} = \gamma B_0$ . To this end, we can apply *Average Hamiltonian Theory* (AHT) in the laboratory frame. AHT is the simplest way of computing the effect of a periodically time-dependent perturbation Hamiltonian, if we can be content with stroboscopic detection (after full periods of length  $T$ ) or if the effect is integrated over a time much longer than the period of the perturbation. The latter is the case here, since the time increment in detection is much longer than  $2\pi/\omega_{\text{nonres}}$ .

AHT is based on the Magnus expansion. For a time interval  $[0, T]$ , the average Hamiltonians  $\overline{\hat{H}}^{(o)}$  with orders  $o = 1 \dots 3$  are computed as

$$\overline{\hat{H}}^{(1)} = \frac{1}{T} \int_0^T \hat{H}(t) dt , \quad (3.8)$$

$$\overline{\hat{H}}^{(2)} = \frac{1}{2iT} \int_0^T dt_2 \int_0^{t_2} [\hat{H}(t_2), \hat{H}(t_1)] dt_1 , \quad (3.9)$$

$$\overline{\hat{H}}^{(3)} = -\frac{1}{6T} \int_0^T dt_3 \int_0^{t_3} dt_2 \int_0^{t_2} \left\{ [\hat{H}(t_3), [\hat{H}(t_2), \hat{H}(t_1)]] + [[\hat{H}(t_3), \hat{H}(t_2)], \hat{H}(t_1)] \right\} dt_1 . \quad (3.10)$$

The Hamiltonian for non-resonant irradiation is

$$\hat{H} = \omega_1 \cos(\omega_{\text{nonres}} t) \hat{S}_x + \omega_1 \sin(\omega_{\text{nonres}} t) \hat{S}_y \quad (3.11)$$

with  $T = 2\pi/\omega_{\text{nonres}}$ . One easily ascertains

$$\overline{\hat{H}}^{(1)} = 0 . \quad (3.12)$$

This is the RWA result. With  $[\hat{S}_x, \hat{S}_y] = \imath \hat{S}_z$ , we find

$$\overline{\hat{H}}^{(2)} = -\frac{\omega_1^2}{\omega_{\text{nonres}}} \hat{S}_z . \quad (3.13)$$

For the special case of the counter-rotating component of the linearly polarized field, we obtain the Bloch-Siegert shift

$$\Delta_{\text{BS}} = \Delta_{\text{BS}}^{(2)} = -\frac{\omega_1^2}{2\omega_{\text{irr}}} . \quad (3.14)$$

Typical values for electron spins at X-band frequencies are  $\nu_1 = 40$  MHz and  $\nu_{\text{irr}} = 9600$  MHz, where we have converted to frequencies  $\nu_i = \omega_i/(2\pi)$ . The Bloch-Siegert shift is then  $\Delta_{\text{BS}} = -0.083$  MHz, which is not usually detectable. Now consider an electron-electron double resonance experiment, where the second frequency is off-resonant by 100 MHz and  $\nu_1 = 10$  MHz. Here, we find  $\Delta_{\text{BS}} = -1$  MHz. If we apply such a pulse for a time  $t_p = 25$  ns ( $\pi/2$  pulse), we induce a phase shift  $\Delta\phi_{\text{BS}} = t_p\Delta_{\text{BS}} = 9^\circ$  on coherence of the off-resonant spins, which is noticeable. This is called a dynamic Bloch-Siegert shift.

If we go beyond second order in AHT and use Eq. (3.10), we obtain as the next Bloch-Siegert shift term,

$$\overline{\hat{\mathcal{H}}}^{(3)} = -\frac{\pi}{2} \frac{\omega_1^3}{\omega_{\text{nonres}}^2} \hat{S}_x. \quad (3.15)$$

If  $\omega_1 \ll \omega_{\text{nonres}}$ , this term is negligible compared to  $\overline{\hat{\mathcal{H}}}^{(2)}$ . On the other hand, if  $\omega_1$  is comparable to or larger than  $\omega_{\text{nonres}}$ , then the Magnus expansion does not converge. We shall come back to this problem when discussing dynamic Bloch-Siegert shift upon passage of a transition.

 [Bri16]

### 3.1.3 Arbitrary Waveform Excitation and Frequency Sweeps

The excitation arm of a magnetic resonance spectrometer generally acts as a low-pass filter. In other words, there is an upper cutoff frequency  $\nu_{\text{max}}$  beyond which excitation power decreases dramatically. Usually the excitation arm even acts as a bandpass, imposing in addition a lower cutoff frequency  $\nu_{\text{min}}$ . Modern spectrometers use Direct Digital Synthesizers (DDS) or Arbitrary Waveform Generators (AWG) as excitation sources. The devices have an upper limit corresponding to about 80% of the Nyquist frequency  $1/(2\Delta t)$  that results from their shortest possible time step  $\Delta t$ . Usually, such devices are characterized by their sampling rate. For instance, a 2 GSa/s AWG has an upper cutoff frequency of approximately 800 MHz. If a signal from such an AWG with at least two output channels is upconverted with an IQ mixer, using a local oscillator (LO) frequency  $\nu_{\text{LO}}$ , the available excitation band is approximately  $\nu_{\text{LO}} \pm 800$  MHz. We shall discuss bandwidth limitations in more detail in Section 3.1.4.

Any real, bandwidth-limited waveform  $y(t)$  can be expressed with an amplitude modulation (AM) function  $\nu_1(t) = \omega_1(t)/(2\pi)$ , a frequency modulation (FM) function  $f(t)$ , and an initial phase  $\phi_0$

$$y(t) = \nu_1(t) \cos \left( \int_0^t f(t') dt' + \phi_0 \right). \quad (3.16)$$

Alternatively, the waveform can be specified with a phase modulation (PM) function  $\phi(t) = \int_0^t f(t') dt' + \phi_0$  as  $y(t) = \nu_1(t) \cos[\phi(t)]$ . If upconversion by an IQ mixer is intended, the corresponding quadrature component is obtained by replacing the cos function by a sin function.

In passage experiments, we are concerned with a special type of arbitrary waveforms, where the FM function  $f(t)$  is monotonous. Such waveforms are called *frequency sweeps*. If  $f(t)$  is monotonously increasing, it is an upward sweep, if it is monotonously decreasing, it is a downward sweep. Frequency sweeps are simpler to treat than general arbitrary waveforms, because each transition in a spin system is passed only once during a single



sweep. Among all frequency sweeps, the simplest one is a linear sweep or *chirp* with rate  $r_{\text{sweep}}$ , where  $f(t) = f_0 + r_{\text{sweep}}t$ .

For any frequency sweep, Fourier transformation of  $f(t)$  and computation of the magnitude spectrum provides an estimate of the excitation band and of uniformity of excitation within this band. Note that excitation of spins is nonlinear in  $\omega_1$ . Hence, the excitation band provided by Fourier transformation is not quantitatively correct, unless small  $\omega_1$  in the *linear regime* are used. The linear regime is usually associated with  $\beta < 30^\circ$ , corresponding to  $\sin \beta < 1/2$ . Merely considering the excitation band neglects phase dispersion of the excited spin packets, which we will discuss in Section 3.2.4.

 [DJ17]

### 3.1.4 Bandwidth Limitations and Deadtime

Bandwidth limitations arise upon generation, amplification, and transmission of high-frequency electromagnetic waves. In the microwave range, low-loss transmission is usually possible only in an octave band. Hence, the upper cutoff frequency is twice the lower cutoff frequency. High-power microwave amplifiers operate in even narrower bands. The most bandwidth-limiting element of a magnetic resonance spectrometer is usually the probehead. Because magnetic interaction is weak, the electromagnetic field is amplified by a resonance circuit (NMR) or microwave resonator (EPR). At its centre frequency  $f_0$ , the resonator enhances the amplitude  $B_1$  of the electromagnetic field by the square root of its loaded quality factor  $Q_L$ <sup>2</sup> *quality factor*.

$$B_1 = \sqrt{\frac{2\mu_0 P_0 Q_L}{V_r f_0}}, \quad (3.17)$$

where  $P_0$  is the incident power and  $V_r$  the effective resonator volume. The enhancement is reciprocal, i.e. the detected voltage at given spin magnetization also increases with the square root of  $Q_L$ . This would suggest to increase the quality factor as much as possible, which is achieved by reducing losses in the resonator. However, the larger  $Q_L$ , the lower is the bandwidth  $\Delta f_{\text{reson}}$

$$\Delta f_{\text{reson}} = \frac{f_0}{Q_L}. \quad (3.18)$$

At  $\pm\Delta f$ , power enhancement is reduced by 3 dB. Hence,  $B_1$  and of the voltage detected at given spin magnetization can depend strongly on frequency difference  $\Delta f$  from the resonator centre frequency. This dependence can be estimated as

$$\frac{B_1(\Omega)}{B_1(0)} \approx \frac{V(\Omega)}{V(0)} = 1/\sqrt{1 + \left(\frac{2\Delta f Q_L}{f_0}\right)^2} \quad (3.19)$$

In applications, it may be useful to determine  $B_1(\Omega)/B_1(0)$  for a given resonator and sample by measuring the dependence of nutation frequency on  $\Delta f$ .

Bandwidth limitation of the resonator is important because it changes the AM function  $\nu_1(t)$  as compared to the amplitude function of the excitation source. Another problem arises, because power stored in the resonator subsides more slowly at lower resonator

<sup>2</sup>The qualifier "loaded" means that the resonator is connected to a transmission line, not that it is loaded with a sample.

bandwidth. This limits detection, since excitation power is by many orders of magnitude larger than signal power. Hence, detection is possible only after a *deadtime* that is related to the resonator rise time  $t_{\text{rise}} = Q_L/f_0$ . For distortion-free detection, we require that the power  $P_0$  initially incident at the resonator decays to below noise power  $P_{\text{noise}}$ . For that, we need to wait for a ringdown time

$$t_{\text{ringdown}} = \frac{Q_L}{f_0} \ln \frac{P_0}{P_{\text{noise}}} . \quad (3.20)$$

For these reasons, microwave resonators are overcoupled for pulsed excitation, which reduces the quality factor below  $Q_L$  of the critically coupled resonator. Such overcoupling is not usually required in NMR, where both the critically coupled  $Q_L$  and the maximum  $\Delta f/f_0$  are lower. In EPR, one usually aims at a compromise between enhancement of the excitation field and resonator bandwidth. Precise spin control then requires resonator compensation of the AM function (Section 3.2.5).

## 3.2 Passage of a Single Transition

### 3.2.1 Linear Frequency Sweep with Constant Amplitude

We consider a linear frequency sweep with constant amplitude  $\omega_1$  from far below resonance ( $-\Omega \gg \omega_1$ ) to far above resonance ( $\Omega \gg \omega_1$ ). The situation is best pictured in an accelerating frame that rotates with instantaneous frequency  $f(t) = f_0 + r_{\text{sweep}}t$ . We further assume  $\phi_0 = 0$ . The accelerating-frame Hamiltonian is then given by

$$\hat{\mathcal{H}}^{(acc)} = \Omega(t)\hat{S}_z + \omega_1\hat{S}_x . \quad (3.21)$$

It is diagonalized by a transformation

$$\hat{\mathcal{H}}^{(acc)} \xrightarrow{\theta\hat{S}_y} \hat{\mathcal{H}}_{\text{EB}}^{(acc)} \quad (3.22)$$

with

$$\theta = \theta(t) = \arctan \frac{\omega_1}{\Omega(t)} \quad (3.23)$$

yielding

$$\hat{\mathcal{H}}_{\text{EB}}^{(acc)} = \omega_{\text{eff}}\hat{S}'_z , \quad (3.24)$$

where the instantaneous  $z'$  axis is in the original  $xz$  plane and includes angle  $\theta$  with the original  $z$  axis. The *effective field* is  $\omega_{\text{eff}} = \sqrt{\Omega^2(t) + \omega_1^2}$ . This situation is illustrated in Fig. 3.1a.

If relaxation is sufficiently slow, the magnetization vector always precesses with frequency  $\omega_{\text{eff}}$  around the instantaneous  $z'$  axis. If the change of orientation of the  $z'$  axis is always slow compared to  $\omega_{\text{eff}}$ , opening of the precession cone will remain small. In other words, to a good approximation the magnetization vector will follow the effective field. Such *adiabatic passage* is illustrated in Fig. 3.1b. If, on the other hand, the frequency sweep and thus the orientation change is faster, then a precession cone will open up. Such *fast passage* is illustrated in Fig. 3.1c. The same passages are visualized in Fig. 3.2 in a frame rotating with the resonance frequency of the passed transition. In this case, the magnetization vector becomes stationary at the end of the fast-passage sweep although coherence was generated. This is because the frame rotates with the resonance frequency of the transition, so that coherence on this transition does not gain phase in this frame.

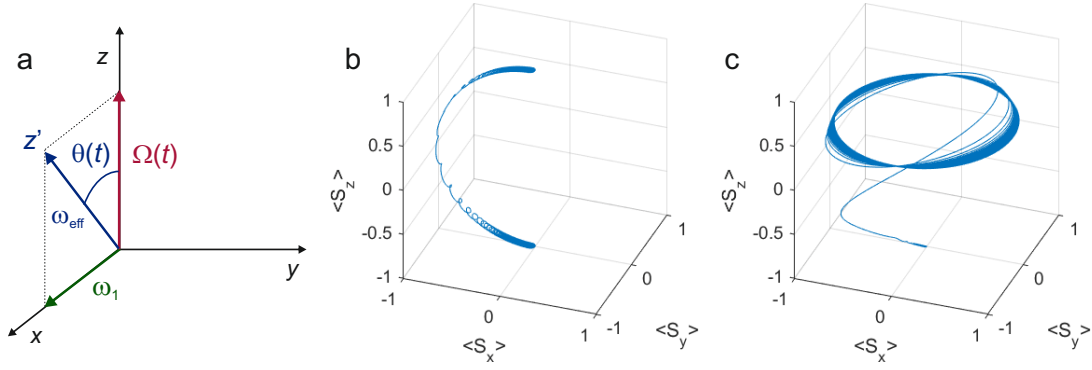


Figure 3.1: Passage of a single transition during a constant-amplitude linear frequency sweep visualized in an accelerated frame. Simulations are for a sweep from -100 MHz below resonance to 100 MHz above resonance in 25  $\mu$ s. An electron spin with  $\langle \hat{S}_z \rangle(0) = -1$  is assumed. Panels b and c can be generated with Matlab script `passage_accelerated_frame.m` (a) Accelerated-frame representation of local fields. (b) Adiabatic passage with  $\nu_1 = 5$  MHz. (c) Fast passage with  $\nu_1 = 1$  MHz.

### 3.2.2 Adiabaticity and Flip Angle upon Passage

For prediction of experimental outcomes, we need to quantify the concepts of adiabatic and fast passage. *Adiabaticity*  $Q(t)$  is defined as the ratio between the effective field  $\omega_{\text{eff}}$  and the rate of change of orientation of this field in the accelerated frame,  $d\theta/dt$ .

$$Q(t) = \frac{\omega_{\text{eff}}}{|d\theta/dt|} = \frac{\sqrt{\omega_1^2 + \Omega^2}}{|d\theta/dt|} = \frac{\sqrt{\omega_1^2 + \Omega^2}}{|\omega_1 (d\Omega/dt) - \Omega (d\omega_1/dt)|}. \quad (3.25)$$

Adiabatic passage corresponds to  $Q \gg 1$ . In practice,  $Q \geq 5$  provides a good approximation, as we shall see shortly. An adiabatic pulse inverts the spin state. For polarization, this is visualized in Fig. 3.1 and 3.2. The concept applies beyond polarization. For coherence, phase is inverted with respect to an axis in the  $xy$  plane. In operator notation, adiabatic passage interconverts between  $\hat{S}^+$  and  $\hat{S}^-$ . Thus, adiabatic passage is equivalent to a  $\pi$  pulse or 180° degree pulse.

In general, adiabaticity  $Q$  according to Eq. (3.25) varies during the sweep. For a chirp pulse with constant  $d\Omega/dt$  and constant  $\omega_1$ ,  $Q(t)$  is minimum at time  $t_0$  of passage ( $\Omega = 0$ ). Adiabaticity upon passage is thus critical for determining the adiabaticity of the whole sweep. Therefore, we refer to it as *critical adiabaticity*  $Q_{\text{crit}}$ . We find

$$Q_{\text{crit}} = \frac{\omega_1}{|d\Omega/dt|} \Big|_{t_0} = \frac{\omega_1}{|d\omega/dt|} \Big|_{t_0}, \quad (3.26)$$

where  $\omega(t) = 2\pi f(t)$  is the FM function in angular frequency units.

We continue by considering a linear sweep with constant amplitude  $\omega_1$  of the irradiation and define the *sweep rate*  $r_{\text{sweep}} = 2\pi df/dt$ . With that we have

$$Q_{\text{crit}} = \frac{\omega_1^2}{r_{\text{sweep}}}. \quad (3.27)$$

The effect of such passage on a Zeeman eigenstate has been considered independently by Landau, Zener, Stückelberg, and Majorana. Phrased for a initial state  $-\hat{S}_z$ , their derivations arrive at an inversion efficiency

$$I_{\text{LZSM}} = \frac{1}{2} + \langle \hat{S}_z \rangle = 1 - e^{-\pi Q_{\text{crit}}/2}. \quad (3.28)$$

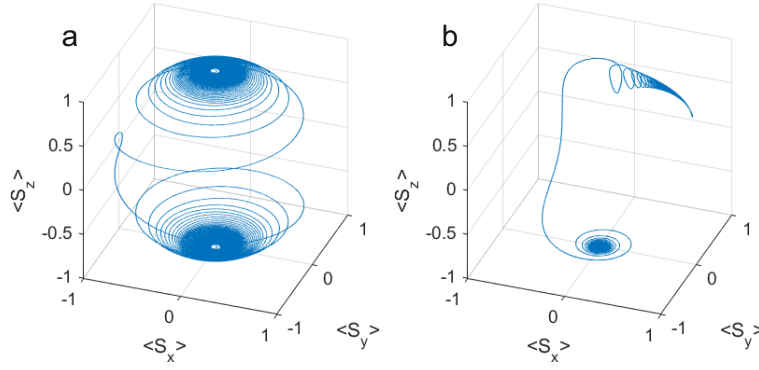


Figure 3.2: Passage of a single transition during a constant-amplitude linear frequency sweep visualized in a frame rotating with the resonance frequency. Simulations are for a sweep from -100 MHz below resonance to 100 MHz above resonance in 25  $\mu\text{s}$ . An electron spin with  $\langle \hat{S}_z \rangle(0) = -1$  is assumed. Panels b and c can be generated with Matlab script `passage_rotating_frame.m` (a) Adiabatic passage with  $\nu_1 = 5$  MHz. (b) Fast passage with  $\nu_1 = 1$  MHz.

Since the effect of passage is a state space rotation, the righthmost expression for  $I_{\text{LZSM}}$  applies to any inversion of spin state, including coherence. We can thus define an equivalent flip angle

$$\beta_{\text{LZSM}} = \arccos \left( 2e^{-\pi Q_{\text{crit}}/2} - 1 \right) . \quad (3.29)$$

Maximum coherence generation from a Zeeman eigenstate corresponds to  $\beta_{\text{LZSM}}$  ( $90^\circ$  pulse) and thus to  $Q_{\text{crit}} = 2 \ln(2) / \pi \approx 0.4413$ . For  $Q_{\text{crit}} = 5$ , we find a flip angle of  $177.7^\circ$ , which is often sufficiently close to perfect inversion.

**L** [DJ17]

### 3.2.3 Offset-independent Adiabaticity

We still consider a spin system with a single transition, where now transition frequency  $\omega_0$  is distributed. Such distribution can arise, for instance, for an electron spin  $S = 1/2$  with substantial  $g$  anisotropy. In this case, the distribution of  $\omega_0$  results different orientations of the principal axes frame of the  $g$  tensor with respect to the static field. All spins in the sample with the same  $\omega_0$  constitute a *spin packet*. In any rotating frame, different spin packets have different offset frequencies. Upon passage, they will behave the same if and only if they have the same  $Q_{\text{crit}}$ . For a linear, constant-amplitude sweep (chirp), this applies according to Eq. (3.27), provided that the sweep starts well below the minimum resonance frequency of all spin packets and ends well above their maximum resonance frequency.

For general FM and AM functions,  $Q_{\text{crit}}$  may vary among spin packets. This is usually undesirable. Often, it is thus advantageous to employ FM/AM function pairs that lead to offset-independent adiabaticity (OIA) [TG96]. In addition to the chirp, two OIA pulses are of special interest.

#### Generalized Hyperbolic Secant Pulse

The generalized hyperbolic secant (HS) pulse has an AM function

$$\nu_1^{\text{HS}n}(t) = \nu_{1,\text{max}} \operatorname{sech}(\tilde{t}^n 2^{n-1} \beta) , \quad (3.30)$$

where  $n$  is the order of the HS pulse,  $\tilde{t} = (t - t_{\text{centre}})/t_{\text{pulse}}$  is a normalized time variable that ranges from -0.5 to 0.5, and  $\beta$  is an apodization parameter (see Section 3.2.3). The normalized time variable is defined with the pulse length  $t_{\text{pulse}}$  and the pulse centre time  $t_{\text{centre}}$ . The corresponding FM function is given by

$$f^{\text{HS}n}(t) = f_{\text{min}} + \Delta f \frac{\int_{-0.5}^{\tilde{t}} \text{sech}(\tau^n 2^{n-1} \beta d\tau)}{\int_{-0.5}^{0.5} \text{sech}(\tau^n 2^{n-1} \beta d\tau)}, \quad (3.31)$$

where  $f_{\text{min}}$  is the initial frequency of the sweep and  $\Delta f$  is the width of the frequency sweep.

The most widely applied hyperbolic secant pulse has  $n = 1$  and provides particularly steep edges of the excitation band in frequency domain. In other words, spin packets in the range  $(f_{\text{min}}, f_{\text{min}} + \Delta f)$  are nearly uniformly excited, whereas spin packets outside this range are nearly unexcited. This property is desirable if several non-overlapping excitation bands are needed for an experiment. The HS pulse achieves it at the expense of a much lower critical adiabaticity  $Q_{\text{crit}}$  than is obtained with a chirp pulse at the same maximum excitation power. If the application is excitation-power limited, it may be advantageous to use higher-order HS pulses ( $n \geq 1$ ). They lead to more gentle edges of the excitation band, but higher  $Q_{\text{crit}}$  at given  $\nu_{1,\text{max}}$  and pulse length  $t_{\text{pulse}}$ .

It is possible to apply different orders  $n$  to the two halves of a HS pulse ( $\tilde{t} \leq 0$  and  $\tilde{t} > 0$ ). This is useful if the facing excitation band edges need to be steep, whereas the far-side edges can be more gentle.

### Gaussian Pulse

Some experiments rely on very gently sloping excitation bands. Such excitation bands can be achieved by a Gaussian AM function,

$$\nu_1^{\text{Gauss}}(t) = \nu_{1,\text{max}} \exp\left(\frac{-\beta^2 \tilde{t}^2}{2}\right). \quad (3.32)$$

The corresponding FM function for achieving OIA is

$$f^{\text{Gauss}}(t) = \frac{\text{erf}(\beta \tilde{t})}{\text{erf} \beta}. \quad (3.33)$$

### Apodization of the AM Function

The AM functions of HS and Gaussian pulses decay to zero only at normalized times  $\tilde{t} \rightarrow -\infty$  and  $\tilde{t} \rightarrow \infty$ . The AM function of a chirp pulse does not decay at all. Since a pulse necessarily has finite length  $t_{\text{pulse}}$ , this leads to amplitude jumps at the beginning and end of the pulse. At first sight, this does not appear to cause problems, since exactly such jumps are the hallmark of rectangular monochromatic pulses. Such pulses were used exclusively before the advent of frequency-swept pulses and they are still widely used in magnetic resonance. However, frequency-swept pulses are often applied in a context where the excitation band should be smooth. The jumps cause ripples both outside and inside the intended frequency range. It is often desirable to reduce the amplitude of these ripples.

In the linear excitation regime, the problem is formally equivalent to filter design. It is also equivalent to avoidance of ripples in discrete Fourier transformation when a signal has not decayed at maximum observation time  $t_{\text{max}}$ . The standard solution for the latter problem is multiplication of the experimental signal with an apodization window function before applying Fourier transformation.

For HS and Gaussian pulses, the parameter  $\beta$  governs such apodization. For HS pulses,  $\beta = 10$  strikes a good compromise between ripple avoidance and loss in steepness of the

excitation band edges. Chirp pulses can be apodized with a quarter sine window function

$$w(t) = \sin\left(\frac{\pi t}{2t_{\text{rise}}}\right) \quad (t \leq t_{\text{rise}}) \quad (3.34)$$

at the leading pulse edge. An analogous quarter sine function is applied at the trailing edge. The rise time  $t_{\text{rise}}$  determines quality of ripple suppression. The minimum and maximum offset resonance frequencies of spin packets should be inside the constant-amplitude range of the AM function ( $t \geq t_{\text{rise}}$  and  $t \leq t_{\text{pulse}} - t_{\text{rise}}$ ).

### WURST Pulse

Instead of using quarter-sine apodization at the time-domain edges of the pulse, one can apply a continuous envelope function to the whole pulse. This is the idea behind wideband, uniform-rate smooth truncation (WURST)<sup>3</sup> pulses. The AM function of WURST pulses is defined as

$$\nu_1^{\text{WURST}}(t) = \nu_{1,\text{max}} (1 - \sin^n(\pi \tilde{t})) \quad , \quad (3.35)$$

where larger  $n$  correspond to less apodization. Strictly speaking, WURST pulses do not achieve OIA. However, at sufficiently large  $n$ , OIA is reasonably well approximated for a large fraction of the sweep.

 [DJ17]

### 3.2.4 Phase Dispersion and Echo Refocusing

Whereas the concept of OIA can ensure uniform excitation of spin packets with respect to flip angle, transverse magnetization after a frequency-swept pulse is not phase coherent between spin packets. This is because spin packets are excited at different times during the sweep and henceforth acquire phase according to their resonance frequency  $\omega_0$ . For an upward chirp pulse, excitation of coherence can be referenced to the time  $t_0$  of passage. The time between excitation and the end of the pulse is

$$\Delta t(\omega_0) = t_{\text{pulse}} - t_0(\omega_0) = \frac{f_{\text{final}} - \omega_0/(2\pi)}{\Delta f} t_{\text{pulse}} \quad , \quad (3.36)$$

where  $f_{\text{centre}}$  is the centre frequency of the sweep. The phase acquired until the end of the pulse is the product of  $\omega_0$  and  $\Delta t(\omega_0)$ , which leads to a parabolic dependence of phase on  $\omega_0$ .

Coherence of all spin packets can be brought in phase by an echo experiment. Consider an echo experiment that consists of two chirp pulses. After the second pulse, the dependence of phase on  $\omega_0$  must be linear, i.e., of the form  $\phi(\omega_0) = -\tau(\omega_0 - \omega_{\text{RF}})$  with a positive constant  $\tau$ . Here,  $\omega_{\text{RF}}$  is the angular frequency of frame rotation that corresponds to the frequency of downconversion. In the time  $t$  after the pulse, spin packets gain phase  $(\omega_0 - \omega_{\text{RF}})t$ , so that they all have phase 0 at time  $t = \tau$ . In a frame rotating with another fixed frequency, phase will not be zero, but it will still be the same for all spin packets.

How we can ensure such linear dependence of phase on frequency after the second pulse? We can disregard the time that passes between the two chirp pulses, as phase gain during free evolution is frequency-linear. If we assume that the two pulses sweep through the same frequency range, the problem thus boils down to determining the length of the second pulse

<sup>3</sup>The envelope has the shape of a sausage, which in German is a "Wurst"

that leads to linear dependence of phase on frequency. We parametrize the problem by a ratio  $r$  between the length of the second pulse and the length  $t_{\text{pulse}}$  of the first pulse. Before inversion during the second pulse, the spin packet gains phase

$$\Delta\phi_1 = \omega_0\Delta t(\omega_0) + r\omega_0(t_{\text{pulse}} - \Delta t(\omega_0)) . \quad (3.37)$$

Upon passage during the second pulse, the sign of  $\Delta\phi_-$  is inverted. Until the end of this pulse, the coherence gains new phase

$$\Delta\phi_2 = r\omega_0\Delta t(\omega_0) . \quad (3.38)$$

We find

$$-\Delta\phi_1 + \Delta\phi_2 = -r\omega_0 t_{\text{pulse}} - \omega_0\Delta t(\omega_0)(2r - 1) . \quad (3.39)$$

The first term on the right-hand side of Eq. (3.39) is the wanted term with linear dependence of a negative phase on frequency. The second term introduces a parabolic dependence and must thus vanish for all  $\omega_0$ . This can be achieved only for  $r = 1/2$ .

For multi-pulse echoes, the refocusing condition for chirp pulses can be generalized to

$$\sum_l s_l t_{\text{pulse},l} (o_l^- - o_l^+) = 0 , \quad (3.40)$$

where index  $l$  runs over all pulses,  $s_l$  is a sign factor that is positive for upward sweeps and negative for downward sweeps, and  $o_l^-$  and  $o_l^+$  are coherence orders before and after the pulse with index  $l$ , respectively. For the two-pulse echo considered above, we have  $s_1 = s_2 = 1$ ,  $o_1^- = 0$ ,  $o_1^+ = o_2^- = 1$ , and  $o_2^+ = -1$ . Hence, the condition is

$$-t_{\text{pulse},1} + t_{\text{pulse},2} + t_{\text{pulse},2} = 0 , \quad (3.41)$$

which yields  $t_{\text{pulse},2} = t_{\text{pulse},1}/2$  as expected.

### Bloch-Siegert Phase and ABSTRUSE Refocusing

Up to this point, our treatment neglected dynamic Bloch-Siegert shift (Section 3.1.2). Such neglect is not a good approximation for passage. During the frequency sweep, we have  $\omega_{\text{nonres}} = \Omega$ , so that  $\omega_1/\omega_{\text{nonres}}$  can become large. In fact, this ratio becomes infinite upon passage at  $t_0$ . The AHT treatment of Bloch-Siegert shift thus breaks down near passage. Fortunately, we can nevertheless estimate the dependence of phase accumulated due to dynamic Bloch-Siegert shift, at least in the OIA case. To this end, we assume that in the range of offsets  $\Omega$ , where AHT breaks down, all spin packets gain the same Bloch-Siegert phase  $\Delta\phi_{\text{pass}}^{\text{BS}}$ . This approximation is good if this breakdown range is well within the total frequency sweep for all spin packets under consideration. Outside this breakdown range, the dependence of Bloch-Siegert phase on spin packet frequency  $\omega_0$  can be computed by integrating Eq. (3.14). After a lengthy derivation [DJ17] this yields

$$\Delta\phi_{\text{BS,OIA}}^{(2)} = \frac{Q_{\text{crit}}}{2} \left\{ C - \ln \left[ \frac{1}{4} - \left( \frac{\omega_0/(2\pi) - f_{\text{centre}}}{\Delta f} \right)^2 \right] \right\} , \quad (3.42)$$

where  $C$  is an unknown constant. At given critical adiabaticity and at a given sweep range, determined by  $\Delta f$  and  $f_{\text{centre}}$ , the result does not depend on pulse length. This indicates that Bloch-Siegert phase can be refocused without interfering with the condition put by Eq. (3.40). However, since Bloch-Siegert phase depends linearly on critical adiabaticity  $Q_{\text{crit}}$ , it may be necessary to adjust amplitude ratio of pulses.

The simplest pulse sequence that refocuses Bloch-Siegert phase is the ABSTRUSE scheme [CSS02], which realises a three-pulse refocused echo with OIA pulses. The pulse length ratio of 2:2:1 for the  $\pi/2$  excitation pulse and the two  $\pi$  inversion pulses fulfils Eq. (3.40). Under the condition that Bloch-Siegert phase during the  $\pi/2$  pulse is negligible, this scheme also refocuses Bloch-Siegert phase. For a stimulated echo, refocusing of Bloch-Siegert phase can be achieved with pulse length ratio 1:2:1 if the first two pulses are downward sweeps and the last pulse is an upward sweep.

### 3.2.5 Resonator Compensation

Critical adiabaticity according to Eq. (3.27) depends quadratically on  $\omega_1$ ,<sup>4</sup> i.e., it is linear in irradiation power. Hence, OIA and Bloch-Siegert phase depend on fidelity of the AM function at the position of the excited spins. Spatial inhomogeneity of the irradiation field often cannot be avoided and causes a distribution of flip angles. This does not interfere with OIA nor with refocusing of Bloch-Siegert phase at a given position in the resonator. For EPR experiments, the frequency-dependent attenuation of  $\nu_1 = \gamma B_1/2\pi$ , as described by Eq. (3.19), is usually more damaging.

The fidelity of the AM function can be restored by compensating the waveform for resonator effects. To this end, one first determines the dependence  $\tilde{\nu}_1(f)$  of the amplitude at the sample for frequency-independent irradiation power. This can be done by measuring the frequency of Rabi oscillations, for instance by a nutation echo experiment. The function  $\tilde{\nu}_1(f)$  is proportional to the magnitude response  $M(f)$  of the resonator.<sup>5</sup> With the AM function  $\nu_1(t)$  at infinite resonator bandwidth, we can then estimate the AM function  $\tilde{\nu}_1(t)$  inside the resonator

$$\tilde{\nu}_1(t) = \nu_1(t) M(f)|_{f=f(t)} . \quad (3.43)$$

If we intend OIA excitation, we can compensate this attenuation by either dividing the input AM function by  $M(f)$  or by adjusting the FM function. The first approach often reduces critical adiabaticity substantially, if  $Q_{\text{crit}}$  is limited by maximum available irradiation power. It may, however, be advantageous if the AM function has some similarity to the shape of the resonator profile.

#### Compensation by an Adapted FM Function

If an excitation bandwidth beyond resonator bandwidth is desired, it is advantageous to compensate the FM function. This is achieved by sweeping more slowly at low  $M(f)$  and sweeping faster at high  $M(f)$ . For a discrete FM function  $\vec{f}$  with  $N$  elements  $f_i$  ( $i = 1 \dots N$ ), we can compute the time of passage of an element  $f_i$  as [DJ17]

$$t(f_i) = \frac{Q_{\text{crit,corr}}}{2} \sum_{k=1}^i \left[ M(f_k) \cdot \nu_1(t)|_{t=t(f_k)} \right]^{-2} . \quad (3.44)$$

The corrected critical adiabaticity is given by

$$Q_{\text{crit,corr}} = \frac{2\pi t_{\text{pulse}}}{\sum_{k=1}^N \left[ \nu_{1,\text{max}} M(f_k) \cdot \nu_1(t)|_{t=t(f_k)} \right]^{-2}} . \quad (3.45)$$

The compensated FM function is then found by inverting  $t(f_i)$  to  $f(t_j)$  and the AM function is provided by interpolating  $\nu_1(t)$  to the  $t_j$ .

<sup>4</sup>While Eq. (3.27) applies strictly only to chirp pulses, the quadratic scaling applies to other frequency sweeps, too.

<sup>5</sup> $M(f) = \tilde{\nu}_1(f) / \max(\tilde{\nu}_1)$



L [DJ17]

### 3.3 Passage in Multi-level Systems

#### 3.3.1 Sequential Single-passage Approximation

Passage of a pair of transitions in a multi-level system can lead to interference. Such interference will generally occur if the two transitions share a level. If this is not the case, interference may still occur if before passage levels the two transitions are connected by coherence. If neither of these conditions is met, the transitions are independent. For independent transitions, it does not matter in which sequence they are passed. Even simultaneous passage can then be treated as two independent passage events on the two transitions. In the other cases, we can apply our understanding of passage of a single transition if passage of the first transition at  $\omega_0^{(1)}$  is complete before the second transition at  $\omega_0^{(2)}$  is affected. This is the case if  $\max(\omega_1) \ll \omega_0^{(2)} - \omega_0^{(1)}$ , where  $\max(\omega_1)$  is the maximum irradiation amplitude during passage of both transitions. In this regime, we can treat the passage of the two transitions as two sequential passages of single transitions.

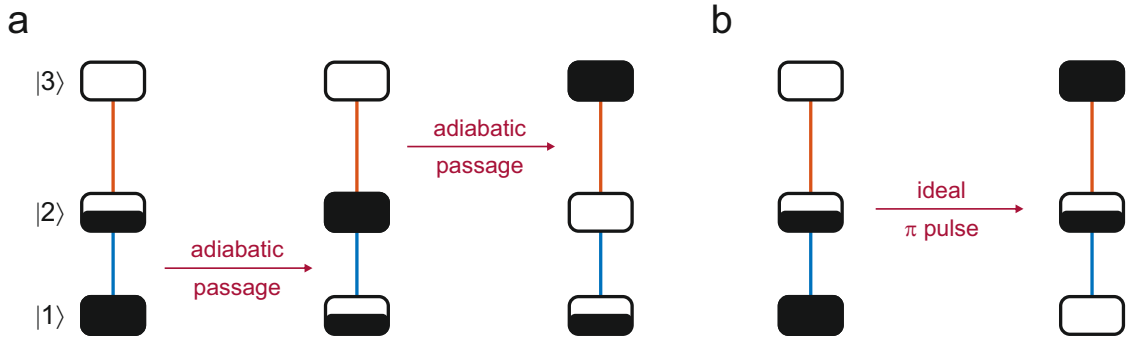


Figure 3.3: Difference between ideal-pulse and adiabatic-passage inversion of a spin-1 system. (a) Longitudinal interference leading to polarization transfer during adiabatic passage of the two transitions of a spin-1 system. Passage of the first transition doubles polarization of the second transition. Upon passage of the second transition, this polarization is inverted and original polarization on the first transition is restored. (b) Application of an ideal (infinitely short monochromatic) pulse affects both transitions equally.

#### 3.3.2 Longitudinal Interference

Longitudinal interference arises because passage of the first transition (transition  $|1\rangle \leftrightarrow |2\rangle$ ) in Figure 3.3a) changes the population of the common level of the two transitions (level  $|2\rangle$ ) in Figure 3.3a). In contrast, polarization of both transitions is inverted by an ideal  $\pi$  pulse (Figure 3.3b). One easily confirms that, for the frequency-swept pulse, the result of upward and downward sweeps is different.

Numerical simulation of chirp pulse excitation well in the sequential passage regime ( $\omega_1/(\omega_0^{(2)} - \omega_0^{(1)}) \approx 0.018$ ) confirms this simple picture of longitudinal interference (Figure 3.4a). Unexpectedly, subsequent inversion of the two transitions is no longer perfect at  $\omega_1/(\omega_0^{(2)} - \omega_0^{(1)}) \approx 0.056$  (Figure 3.4b) where the sequential passage approximation should still hold. As marked by the arrows, the distortion occurs at the centre of the sweep where none of the two transitions is resonant. We defer discussion of the reason to Section 3.3.4. Already at  $\omega_1/(\omega_0^{(2)} - \omega_0^{(1)}) \approx 0.18$  (Figure 3.4c), the sequential passage approximation is

significantly violated. If  $\omega_1$  is of the order of the difference of the two resonance frequencies, neither the individual transitions nor the whole system are properly inverted (Figure 3.4d).

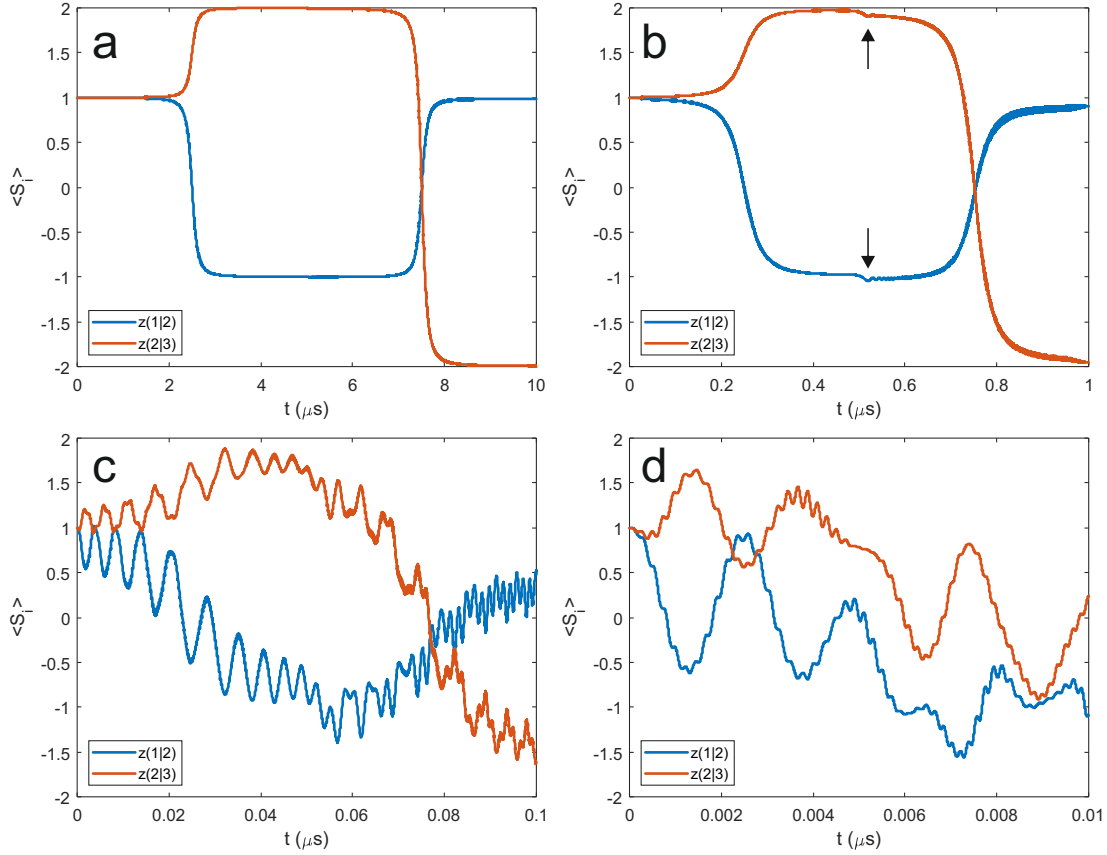


Figure 3.4: Effects of simultaneous excitation of connected transitions during a chirp pulse with  $Q_{\text{crit}} = 5$ . An  $S = 1$  system with zero-field splitting of  $-250 \text{ MHz}$  is assumed and frequency range from  $-500 \text{ MHz}$  to  $500 \text{ MHz}$  around the centre frequency of the two transitions is swept. The polarization on transition  $|1\rangle \leftrightarrow |2\rangle$  (blue) and  $|2\rangle \leftrightarrow |3\rangle$  (brickred) is plotted as function of time after begin of the pulse. (a) Pulse length  $t_{\text{pulse}} = 10 \mu\text{s}$  corresponding to  $\nu_1 = 8.9 \text{ MHz}$ . (b)  $t_{\text{pulse}} = 1 \mu\text{s}$ ,  $\nu_1 = 28.2 \text{ MHz}$ . Arrows denote an effect due to two-photon excitation of the double-quantum transition. (c)  $t_{\text{pulse}} = 100 \text{ ns}$ ,  $\nu_1 = 89.2 \text{ MHz}$ . (d)  $t_{\text{pulse}} = 10 \text{ ns}$ ,  $\nu_1 = 282 \text{ MHz}$ .

### 3.3.3 Transverse Interference

Interference between subsequent passages becomes more complicated if coherence is generated. Passage of the first transition proceeds as in a two-level system, converting all polarization on the transition to coherence and equalizing the populations of the two levels (Figure 3.5a, left). This leads to larger polarization of the second transition and subsequently to larger coherence on this transition after it has been passed. In the high-temperature approximation, where the two polarizations are equal before the sweep, coherence on the second transition is 1.5 times as large as after passage of a single transition.

Coherence on the first transition is reduced when the second transition is passed. This is because, in a three-level system, a pulse applied to transition  $|2\rangle \leftrightarrow |3\rangle$  transfers coherence on transition  $|1\rangle \leftrightarrow |2\rangle$  to coherence on the double-quantum transition  $|1\rangle \leftrightarrow |3\rangle$ . This transfer is complete at flip angle  $\pi$ , i.e., for adiabatic passage of transition  $|2\rangle \leftrightarrow |3\rangle$ .

In Figure 3.5 we assume a flip angle of  $\pi/2$  on the single-quantum transitions. In this situation, only half of the coherence on transition  $|1\rangle \leftrightarrow |2\rangle$  is transferred to double-quantum coherence. Note that, in the  $S = 1$  system that we assumed for the simulation in Figure 3.5b, a  $\pi/2$  pulse at single-quantum transitions requires  $Q_{\text{crit}} = \ln 2/\pi$ . This is only half the value of  $Q_{\text{crit}}$  that effects a  $\pi/2$  pulse in an  $S = 1/2$  system. The difference arises because the transition moment on individual transitions is larger by a factor of  $\sqrt{2}$  in the  $S = 1$  system.

In Figure 3.5b only amplitude of the coherence is plotted, disregarding phase. Prediction of the phase is complicated by dynamical Bloch-Siegert shift (see Section 3.2.4). Details can be found in [DJ17].

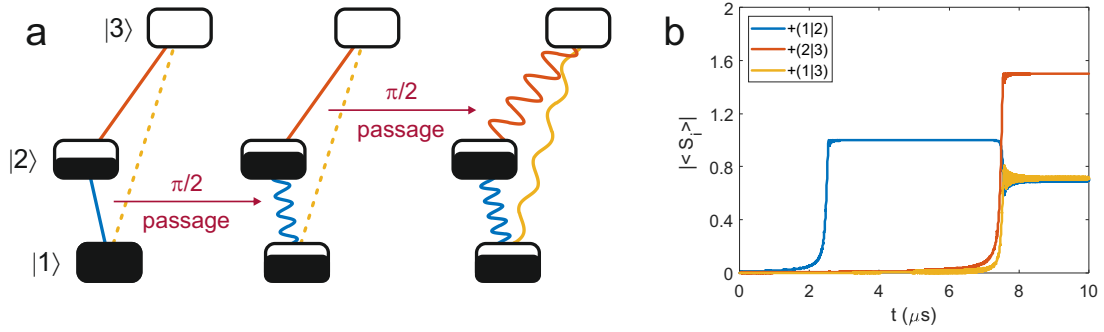


Figure 3.5: Transverse interference upon passage of two transitions that share a level. (a) Passage of the first transition excites coherence on this transition as expected. At the same time, polarization of transition  $|2\rangle \leftrightarrow |3\rangle$  is increased. Passage of the second transition thus creates more coherence on this transition. In addition, this passage transfers part of the coherence on transition  $|1\rangle \leftrightarrow |2\rangle$  to double-quantum coherence on the forbidden transition  $|1\rangle \leftrightarrow |3\rangle$ . (b) A chirp pulse with  $Q_{\text{crit}} = \ln 2/\pi$  is applied, corresponding to a  $\pi/2$  pulse on individual allowed transitions. The amplitude of coherence is plotted versus time, disregarding phase. An  $S = 1$  system with zero-field splitting of  $-250$  MHz is assumed and a frequency range from  $-500$  MHz to  $500$  MHz around the centre frequency of the two transitions is swept. Coherence is generated also on the double-quantum transition  $|1\rangle \leftrightarrow |3\rangle$  (yellow).

### 3.3.4 Multi-photon Transitions

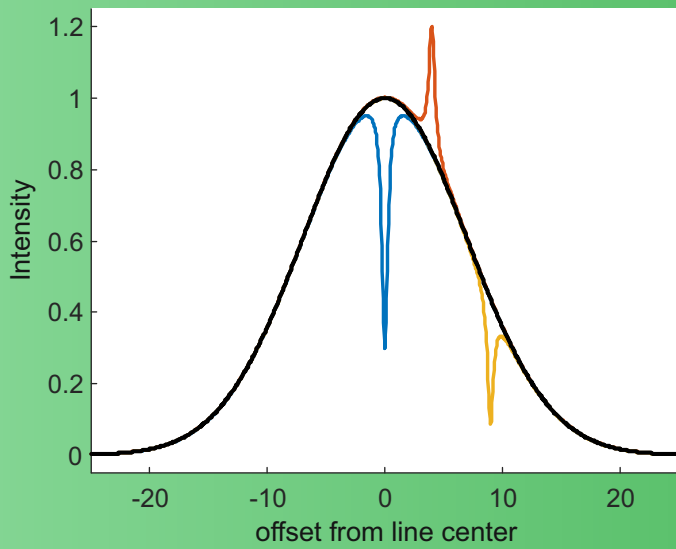
As seen in Figure 3.4b (arrows), resonant state changes may occur in multi-level systems at frequencies that do not correspond to transitions. In the case at hand, the two single-quantum transitions have frequencies of  $33.25$  GHz and  $33.75$  GHz and the double-quantum transition has a frequency of  $67$  GHz. The centre of the sweep, where the state change occurs, is at  $33.5$  GHz. It follows that the spin system absorbs two photons when the double-quantum transition is passed at half its frequency. With an effective nutation frequency  $\omega_{1,\text{DQ}} = 2\omega_1^2/|\omega_{12} - \omega_{23}|$  for the double-quantum transition and an effective sweep rate  $\Delta m_S k$ , one finds [DJ17]

$$Q_{\text{crit,DQ}} = \frac{\omega_{1,\text{DQ}}^2}{\Delta m_S k} = \frac{4w_1^4}{\Delta m_S k |\omega_{12} - \omega_{23}|^2} = \frac{2kQ_{\text{crit}}^2}{|\omega_{12} - \omega_{23}|^2}. \quad (3.46)$$

where we have substituted  $\Delta m_S = 2$ . Similar expressions apply to transitions that involve absorption of more than two photons [Haa+94].

Note that such excitation of forbidden transitions does not require violation of the high-field approximation. If the splitting between two allowed transitions is of the order of

$\omega_1$  or smaller and the two transitions share a level, the process becomes very effective and contributes to breakdown of the sequential single-passage approximation.



## 4. Hole Burning and Shifting

### 4.1 Inhomogeneous Line and Selective Inversion

In the solid state, resonance frequency depends on orientation of the sample with respect to the magnetic field. For electron spins, this dependence arises from  $g$  and hyperfine anisotropy. In high-spin species ( $S > 1/2$ ), anisotropic zero-field splitting also contributes and for electron spin pairs at distances closer than about 20 Å, anisotropy of the dipole-dipole coupling may contribute to the distribution of resonance frequencies. For nuclear spins, the main contributions are chemical shift anisotropy and nuclear dipole-dipole coupling. For nuclear spins  $I > 1/2$ , the main contribution is nuclear quadrupole coupling and for nuclear spins in the vicinity of slowly relaxing electron spins, the main contribution is hyperfine anisotropy. These distributions of resonance frequencies lead to *inhomogeneous line broadening*, as illustrated in Figure 4.1a. Whereas the homogeneous line of a spin packet has Lorentzian shape<sup>1</sup>, the inhomogeneous line shape is determined by the distribution function of the resonance offset, which in turn depends on the anisotropies of all relevant interactions and relative orientation of the principal axes frames of the tensors that describe these asymmetries.

Coming back to the electron spin, the appearance of an inhomogeneous line can even arise in isotropic systems if a sufficiently large number of nuclei with unresolved hyperfine couplings exist. In this case, the role of the spin packets is taken over by individual lines of a hyperfine multiplet of multiplets. Such broadening is called *heterogeneous broadening*. For electron spins in the solid state, usually both inhomogeneous and heterogeneous broadening are relevant. For the following discussion, we do not need to distinguish between these two types of broadening. We use the language of inhomogeneous broadening, where the component at a given resonance frequency is called a spin packet. For simplicity, we assume a Gaussian lineshape with full width at half maximum (FWHM)  $\Gamma_{\text{inh}}$  for the inhomogeneous line and a Lorentzian lineshape with uniform FWHM  $\Gamma_{\text{hom}}$  for the spin packets. In practice,  $\Gamma_{\text{hom}}$  can be anisotropic and can thus vary between spin packets and the inhomogeneous lineshape is rarely Gaussian.

<sup>1</sup>We assume monoexponential transverse relaxation

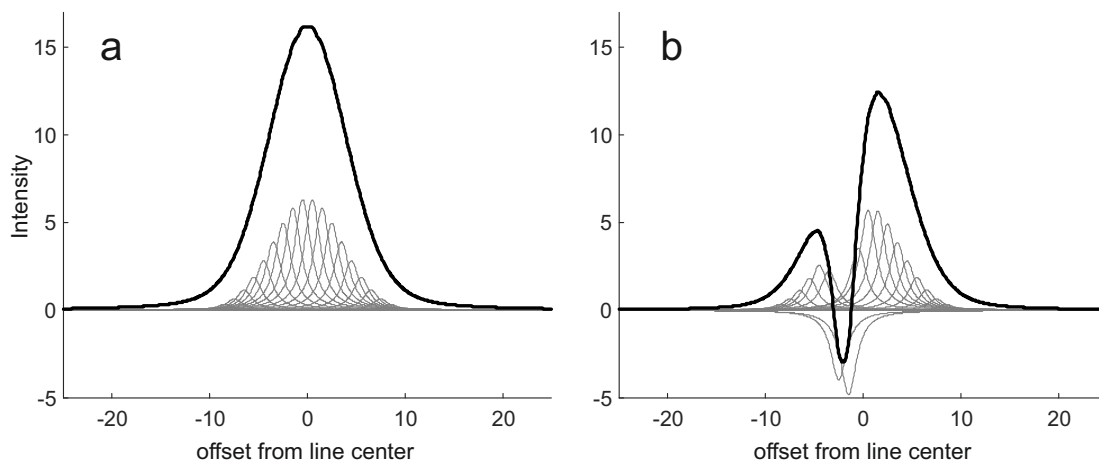


Figure 4.1: Inhomogeneous line and spectral hole burning. (a) Inhomogeneous line (black) resulting from a superposition of 50 spin packets with Lorentzian lines (gray) whose intensity distribution follows Pascal's triangle. (b) Upon selective irradiation at offset -2, spin packets are excited with an efficiency related to their resonance offset. An on-resonance flip angle of  $\pi$  was assumed. Spin packets far off-resonance remain nearly unaffected. As a result, a hole is burned into the inhomogeneous line.

We now assume monochromatic excitation with  $\omega_1 \ll \Gamma_{\text{inh}}$  for time  $t_{\text{pulse}}$  at some frequency within the inhomogeneously broadened line (Figure 4.1b). This is a typical situation in EPR experiments. For an on-resonant flip angle  $\omega_1 t_{\text{pulse}} = \pi$ , spin packets close to the irradiation frequency are almost perfectly inverted. Spin packets with a resonance offset that is much larger than  $\omega_1$  remain nearly unaffected. The result is selective inversion in a narrow range around the irradiation frequency. Quite obviously, this is a means for increasing resolution, since further manipulations can be performed on only the excited spin packets, which correspond to a much narrower line. This resolution enhancement comes at the expense of sensitivity loss, since only a small fraction of all spin packets is excited and detected. The higher the resolution, the lower the sensitivity.

#### 4.1.1 Width and Shape of the Spectral Hole

As is intuitively clear from Figure 4.1, the spectral hole cannot be narrower than the homogeneous line. This limiting linewidth can be achieved only if a single spin packet is excited, which requires  $\omega_1 \ll \Gamma_{\text{hom}}$ . With our assumptions,  $\Gamma_{\text{hom}} = 2/T_2$ , where  $T_2$  is the transverse relaxation time. Thus, the limiting linewidth can only be achieved for  $\omega_1 T_2 \ll 1$ , which implies that inversion is impossible. If the longitudinal relaxation time  $T_1$  is sufficiently long, a *saturation* hole can be burnt at the limiting linewidth. This implies a further loss in sensitivity by a factor of two. Even under these conditions, the limiting linewidth of the hole can be achieved only if *spectral diffusion*<sup>2</sup> is negligible during  $t_{\text{pulse}}$ .

In many cases one is not prepared to accept the sensitivity loss associated with achieving the limiting linewidth. Instead, one strikes a compromise between resolution and sensitivity by selecting an appropriate strength  $\omega_1$  of the irradiation field. The broadening that arises with respect to the limiting hole width is called *power broadening*.<sup>3</sup> The width and the

<sup>2</sup>Spectral diffusion is a change of the resonance frequency that arises mostly from flip-flop processes of spin pairs with similar, but not exactly the same resonance frequency of the two spins. The flip-flops are enabled by the B term of the dipole-dipole coupling between the two spins

<sup>3</sup>We discourage the term "saturation broadening", since saturation can be achieved at the limiting hole width

shape of the hole under power broadening depend on pulse shape, i.e., on the AM function. To a first approximation, which is very good in the linear regime  $\omega_1 t_{\text{pulse}} < \pi/6$ , the shape of the hole corresponds to the Fourier transform of the pulse shape. Hence, rectangular pulses lead to sinc-function-like hole shapes, which include weak side holes. This is detrimental if the hole pattern is later analysed in order to obtain information on Hamiltonian parameters. In such experiments, one seeks smooth hole shapes without side holes, which can be attained by Gaussian-shaped hole-burning pulses. In general, the shape and width of the whole can be sculpted by selecting the AM and FM function. However, if an experiment depends on the observation of frequency shifts or of broadening of individual holes, a monochromatic Gaussian pulse appears to be the optimal choice.

Spectral holes can be detected by application of a  $\pi/2$  pulse and subsequent observation of their free induction decay (*FID-detected hole burning* or by a selective echo experiment. In the former case, it is obvious that in the Fourier transform of the FIF, the hole shape is convoluted with a Lorentzian line whose FWHM on a linear frequency scale is set by  $1/(\pi T_2)$

 [WSS92]

### 4.1.2 Spectral Grating

The smaller width of the spin packets can also be utilized without the large sensitivity loss due to highly selective excitation. To that end, one creates resonance-offset dependent inversion using the pulse sequence  $\pi/2 - \tau - \pi/2$ , where the excitation bandwidth of the  $\pi/2$  pulses either exceeds  $\Gamma_{\text{inhom}}$  or is selected as large as possible. At resonance offsets, where  $\Omega\tau$  is an integer multiple of  $2\pi$ , the phase of magnetization of the spin packet is the same after interpulse delay as directly after the first  $\pi/2$  pulse. Consequently, if the  $\pi/2$  pulses have the same phase, magnetization of the spin packet is inverted. In contrast, if  $\Omega\tau$  is an odd multiple of  $\pi$ , the spin packet has gained phase  $\pi$  before the second  $\pi/2$  pulse. In the absence of relaxation, this pulse then restores the magnetization that existed before the first  $\pi/2$  pulse.

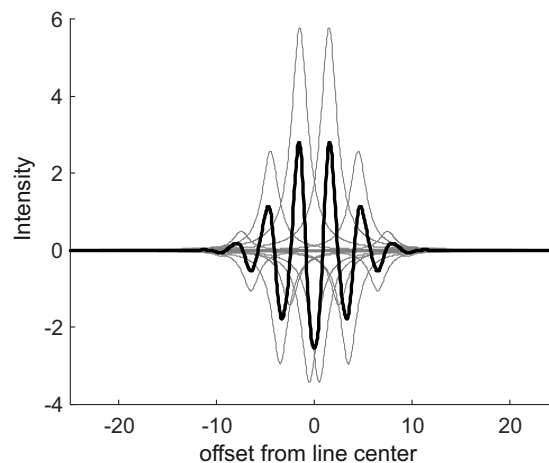


Figure 4.2: Spectral grating in an inhomogeneous line resulting from a superposition of 50 spin packets with Lorentzian lines (gray) whose intensity distribution follows Pascal's triangle. A pulse sequence  $\pi/2 - \tau - \pi/2$  with  $\tau\Delta\nu = 0.3$  was simulated, where  $\Delta\nu$  is the frequency difference between the discrete spin packets.

Figure 4.2 illustrates the result for the same discrete distribution of spin packets that we assumed in Figure 4.1. The pulse sequence generates a cosinoidal polarization grating across the inhomogeneously broadened line. For a continuous distribution of spin packets, the envelope function of the grating is given by the inhomogeneous lineshape and the linear frequency difference between two minima (or maxima) in the grating is  $1/(2\pi\tau)$ . Finesse of the grating is limited by transverse relaxation, since  $\tau$  cannot exceed  $T_2$  by a large factor without losing the magnetization. It can be shown that the optimal interpulse delay for detecting small frequency shifts is given by  $\tau \approx T_2$  [ZJG05].

## 4.2 Hole Burning in Multi-Level Systems

### 4.2.1 Enhanced Hole Burning for Weakly Allowed Transitions

Hole burning allows for enhancing transitions with a small transition moment with respect to transitions with a large transition moment. Small transition moments can arise for formally forbidden transitions in regimes where the magnetic quantum numbers are not strictly good quantum numbers. The transitions are strictly forbidden in the high-field limit, where the Zeeman interactions of all spins exceed all other interactions by a large factor. In this limit, all interactions in the spin Hamiltonian can be truncated to the terms that contain only  $\hat{S}_{z,i}$  and  $\hat{I}_{z,j}$  operators. For interactions between two spins, the limit is only attained if also the difference between their Zeeman interactions - or chemical shift terms - exceeds the interaction strength by far. Notably, this condition is violated for proton pairs in NMR even at the highest magnetic fields that can be attained. If the high-field limit is not attained, some terms that contain spin  $x$  or  $y$  operators are no longer negligible. These terms are referred to as *pseudo-secular* terms. Pseudo-secular terms admix spin states with different sets of magnetic quantum numbers. The corresponding state-space rotation generates off-diagonal elements of the excitation operator, for instance of  $\hat{S}_x$ , that connect formally forbidden transitions.

A case in hand are the electron-nuclear transitions with  $\Delta m_S = 1$ ,  $\Delta m_I = 1$  in the system introduced in example 2.3.1. As demonstrated in the basic magnetic resonance course, the Hamiltonian

$$\hat{\mathcal{H}}_0 = \Omega_S \hat{S}_z + \omega_I \hat{I}_z + A \hat{S}_z \hat{I}_z + B \hat{S}_z \hat{I}_x \quad (4.1)$$

is diagonalized by the transform  $\hat{T}_{\text{EB}} = \exp \left\{ -i \left( \xi \hat{I}_y + \eta 2 \hat{S}_z \hat{I}_y \right) \right\}$  with  $\xi = (\eta_\alpha - \eta_\beta)/2$  and  $\eta = (\eta_\alpha + \eta_\beta)/2$ , where  $\eta_\alpha = \arctan[-B/(2\omega_I + A)]$  and  $\eta_\beta = \arctan[-B/(2\omega_I - A)]$ . In order to assess the effect of excitation in the eigenbasis, we need to apply the same transformation to the excitation term  $\omega_1 \hat{S}_x$ . We find

$$\omega_1 \hat{S}_x \xrightarrow{\hat{T}_{\text{EB}}} \cos(\eta) \hat{S}_x + \sin(\eta) 2 \hat{S}_y \hat{I}_y . \quad (4.2)$$

The term  $\sin(\eta) 2 \hat{S}_y \hat{I}_y$  drives electron-nuclear zero and double-quantum transitions. In most cases,  $\sin \eta \ll \cos \eta$ , i.e., the formally forbidden zero- and double-quantum transitions become only weakly allowed.

#### High Turning-angle Pulses

A pulse with nominal flip angle  $\beta = \omega_1 t_{\text{pulse},0}$  results in smaller flip angles  $\cos(\eta)\beta$  and  $\sin(\eta)\beta$  for formally allowed and forbidden transitions, respectively. This can be compensated by either increasing  $\omega_1$  or prolonging the pulse. Since  $\omega_1$  is limited, one often uses the latter strategy. If  $t_{\text{pulse}}$  is prolonged beyond  $t_{\text{pulse},0}/\cos(\eta)$ , the allowed transitions are "overflipped", i.e., they experience a flip angle larger than  $\beta$ . In the context of hole burning,



the hole due to excitation of allowed transitions reached maximum depth at  $t_{\text{pulse},0}/\cos(\eta)$ . In contrast, the depth of the hole due to excitation of forbidden transitions increases for pulse lengths up to  $t_{\text{pulse},0}/\sin(\eta)$ , if relaxation can be neglected. Power broadening for these holes also scales with  $\sin\eta$ . Because usually  $\sin\eta \ll 1$ , optimal hole-burning pulses for forbidden transitions have flip angle much larger than  $\pi$ . We refer to them as *high turning-angle pulses* (HTA pulses).

### 4.2.2 Side Holes

In a multi-level system, hole burning on one transition will affect polarization of all transitions that share one level with the excited transition. This effect is illustrated in Figure 4.3. We consider a three-level system with energy increasing from level  $|1\rangle$  to  $|3\rangle$ . The frequencies of transitions  $|1\rangle \leftrightarrow |2\rangle$  and  $|2\rangle \leftrightarrow |3\rangle$  are assumed to be very similar (the difference is exaggerated for clarity in Figure 4.3a), so that the frequency of transition  $|1\rangle \leftrightarrow |3\rangle$  is about twice as large. In the high-temperature approximation, transitions  $|1\rangle \leftrightarrow |2\rangle$  and  $|2\rangle \leftrightarrow |3\rangle$  then have about the same thermal equilibrium polarization  $p$ , whereas thermal equilibrium polarization of transition  $|1\rangle \leftrightarrow |3\rangle$  is about twice as large. The populations of the three levels can be assigned as  $1 + p$ ,  $1$  and  $1 - p$ .

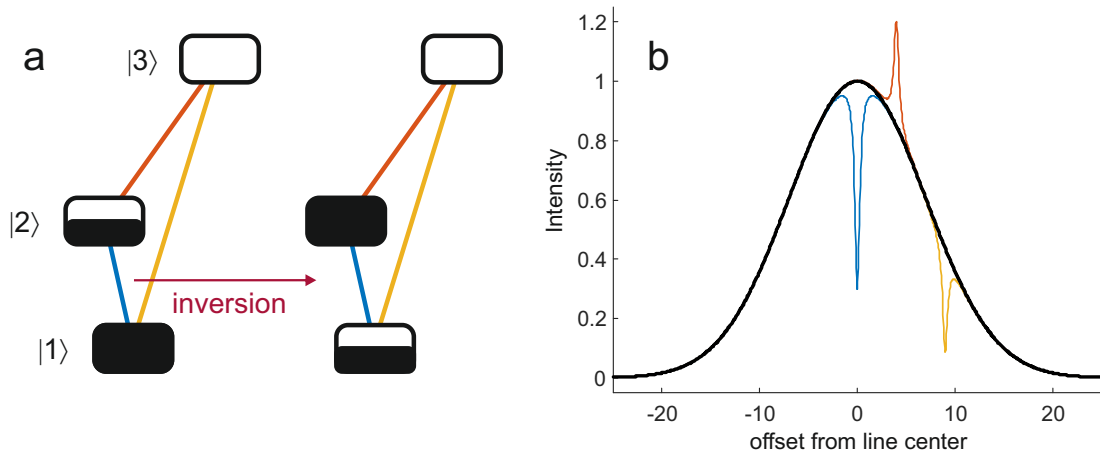


Figure 4.3: Generation of a side hole and antihole in a three-level system. Equal polarization of transitions  $|1\rangle \leftrightarrow |2\rangle$  and  $|2\rangle \leftrightarrow |3\rangle$  is assumed. (a) Upon inversion of transition  $|1\rangle \leftrightarrow |2\rangle$  (blue), polarization of transition  $|2\rangle \leftrightarrow |3\rangle$  (red) doubles, whereas polarization of transition  $|1\rangle \leftrightarrow |3\rangle$  (yellow) halves. Energy differences in the level scheme are exaggerated for clarity. (b) In addition to the central inversion hole at the irradiation frequency (blue), a saturation side hole at the offset frequency of transition  $|1\rangle \leftrightarrow |3\rangle$  (yellow) and an antihole at the offset frequency of transition  $|2\rangle \leftrightarrow |3\rangle$  (red) are generated. In practice, transition  $|1\rangle \leftrightarrow |3\rangle$ , whose frequency is the sum of the frequencies of the two other transitions, may be outside the detection window and may not even be part of the same inhomogeneously broadened line.

Upon inversion of transition  $|1\rangle \leftrightarrow |2\rangle$ , the population of level  $|1\rangle$  decreases by  $p$  to  $1$ , whereas the population of level  $|2\rangle$  increases by  $p$  to  $1 + p$ . This inverts the polarization on this transition from  $p$  to  $-p$ . As a result, transition  $|2\rangle \leftrightarrow |3\rangle$  now has a polarization  $2p$ , which is twice as large as thermal equilibrium polarization. The signal of this transition is enhanced, leading to an antihole as illustrated by the red line in Figure 4.3b. At the same time, the polarization of transition  $|1\rangle \leftrightarrow |3\rangle$ , which originally was  $2p$ , is reduced to  $p$ . This generates a side hole as illustrated by the yellow line in Figure 4.3b.

Depending on the structure of the spin system, only the side hole or only the antihole may be observable. This is because one of the two transitions can be forbidden or in a frequency range outside the detection window or both. For instance, if the three-level system corresponds to a triplet state ( $S = 1$ ) in the high-field approximation, transition  $|1\rangle \leftrightarrow |3\rangle$  is at about twice the microwave frequency and forbidden. If the high-field approximation is slightly violated, this transition is weakly allowed.

 [WJ18]

### 4.2.3 ELDOR-detected NMR

The concepts of enhanced hole burning at forbidden transitions and of generation of side holes are combined in the ELDOR-detected NMR experiment. The situation at thermal equilibrium before the start of the experiment is illustrated in Figure 4.4a. Since the electron Zeeman frequency is much larger than the nuclear Zeeman frequency and the hyperfine couplings, polarization of nuclear-spin transitions (blue) can be neglected. Polarization of both electron-spin transitions (red) is approximately equal. By application of a HTA pulse, the forbidden transition  $|\beta_S\alpha_I\rangle \leftrightarrow |\alpha_S\beta_I\rangle$  can be significantly excited unless  $\sin(\eta)\omega_1 \ll T_2$ .

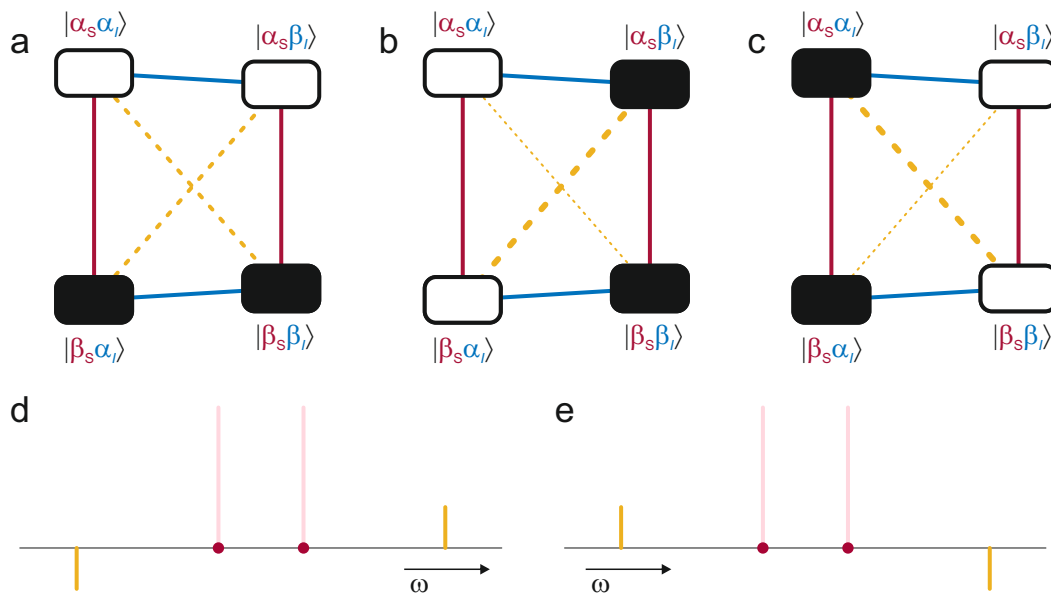


Figure 4.4: Principle of ELDOR-detected NMR. (a) Energy level scheme with box filling corresponding to populations. Electron spin transitions are marked by red solid lines, nuclear spin transitions by blue solid lines, and forbidden electron-nuclear transitions by yellow dashed lines. (b) Inversion of the forbidden transition  $|\beta_S\alpha_I\rangle \leftrightarrow |\alpha_S\beta_I\rangle$  (bold yellow dashed line) equalizes populations on both allowed electron spin transitions. (c) Likewise, inversion of the forbidden transition  $|\beta_S\beta_I\rangle \leftrightarrow |\alpha_S\alpha_I\rangle$  (bold yellow dashed line) equalizes populations on both allowed electron spin transitions. (d) Stick spectrum after inversion of transition  $|\beta_S\alpha_I\rangle \leftrightarrow |\alpha_S\beta_I\rangle$ . Zero signal on the allowed transition corresponds to saturation side holes. (e) Stick spectrum after inversion of transition  $|\beta_S\beta_I\rangle \leftrightarrow |\alpha_S\alpha_I\rangle$ .

In Figure 4.4b we assume that this transition can be inverted. Such inversion equalizes populations in the two level pairs that correspond to the allowed electron spin transitions. The signal of these transitions vanishes (Figure 4.4d). In a hole-burning picture, this corresponds to creation of saturation sideholes that are offset from the excited forbidden

transition by the frequency differences between the forbidden transition and these allowed transitions. One easily ascertains that the frequency differences are the NMR frequencies  $\omega_\alpha$  and  $\omega_\beta$ . The situation is analogous for the other forbidden transition, as illustrated in Figure 4.4c,e. Because the transitions are allowed, the side holes can be detected with high sensitivity.

As discussed above, ELDOR-detected NMR cannot achieve resolution better than twice the homogeneous EPR linewidth. Methods that generate nuclear coherence, such as electron spin echo envelope modulation (ESEEM), or electron nuclear double resonance (ENDOR) techniques can have resolution as good as the homogeneous NMR linewidth. However, if the NMR lines are themselves strongly inhomogeneously broadened, sensitivity of ELDOR-detected NMR can be much better than sensitivity of any of the other techniques.

#### 4.2.4 Solid-effect DNP

The same excitation principle as in ELDOR-detected NMR is used in solid-effect DNP. Figure 4.4a-c illustrates the concept. At thermal equilibrium (panel a), polarization of the nuclear transitions (blue) is negligible compared to polarization of the electron transitions (red). If the electron-nuclear zero-quantum transition is excited (panel b), emissive nuclear-spin polarization is generated for nuclei with positive gyromagnetic ratio, where the  $\alpha_I$  state is the ground state. If the electron-nuclear double-quantum transition is excited (panel c), enhanced absorptive nuclear-spin polarization is generated. If one scans the microwave frequency through the EPR line, sign of the enhanced NMR lines changes. The emissive and absorptive enhancement maxima are split by  $\omega_{\text{alpha}} + \omega_\beta = \sqrt{(\omega_I + A/2)^2 + B^2/4} + \sqrt{(\omega_I - A/2)^2 + B^2/4} \approx 2\omega_I$ .

### 4.3 Hole Shifting

In a multi-level systems, spectral holes can be shifted by applying non-selective or selective pulses to other transitions. We consider three cases for four-level systems.

#### 4.3.1 Non-selective Hole Shifting

We consider a system of two coupled electron spins  $S_1 = 1/2$  and  $S_2 = 1/2$ . The thermal equilibrium spectrum of a single spin packet (bottom of Figure 4.5a) consists of two doublets with the same splitting. This splitting is the coupling between the two spins. In a disordered solid, the centre of the four-line spectrum and the spacing between the two doublets are usually distributed due to anisotropic Zeeman and hyperfine interactions of  $S_1$  and  $S_2$ . Their coupling is also distributed, but this distribution may be much narrower. The latter distribution contains information on the dipole-dipole interaction between  $S_1$  and  $S_2$  as well on their exchange interaction, if present.

If the coupling between the two spins exceeds  $1/T_2$  of spin  $S_1$ , we can selectively excite one of the two transitions of  $S_1$  (Figure 4.5a). In the limit of ideal selectivity, the other transition of  $S_1$  is unaffected. Due to the population changes of the two levels, the connected transitions of spin  $S_2$  are affected, as we discussed in general for multi-level systems in Section 4.2.2. The polarization of one of the transitions of the  $S_2$  doublet is double (antihole) and the polarization of the other transition is zeroed (saturation hole). If the frequency difference between the centres of the  $S_1$  and  $S_2$  doublet were fixed, we could thus resolve the coupling between the two spins as an antiphase hole pattern for spin  $S_2$ . Unfortunately, this frequency difference is usually broadly distributed, leading to cancellation of the antiphase pattern.

We now assume that we can invert the two  $S_2$  transitions without affecting the  $S_1$

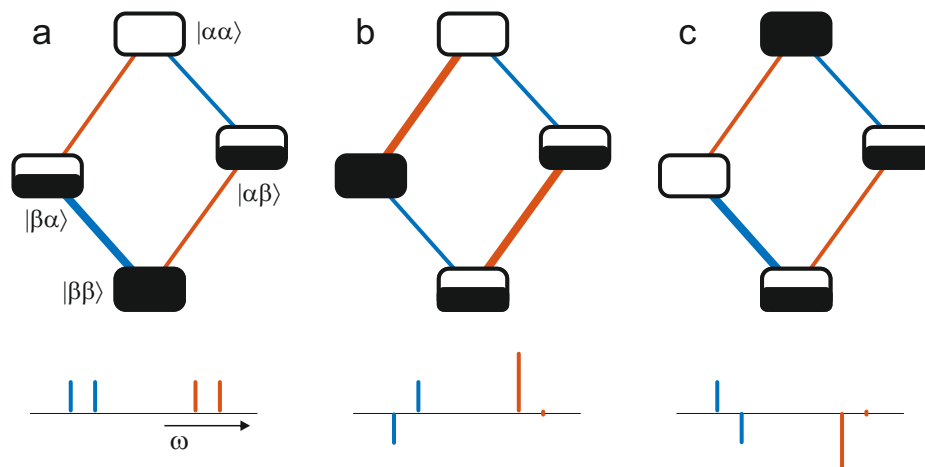


Figure 4.5: Hole shifting by a non-selective pulse. (a) Thermal equilibrium populations (top) and stick spectrum (bottom) for a system of two coupled electron spins  $S_1 = 1/2$  (blue transitions) and  $S_2 = 1/2$  (red transitions). The bold blue line denotes the transition where a hole is burnt. (b) Situation after hole burning on one transition of spin  $S_1$ . The other transition of spin  $S_1$  is unaffected. Of the two transitions of spin  $S_2$  one exhibits enhanced absorption (antihole), whereas for the other one the two populations are equalised, corresponding to a saturation hole. Spin  $S_2$  is now non-selectively inverted (bold red lines). (c) Situation after non-selective inversion of  $S_2$  transitions. The hole on spin  $S_1$  has been shifted by the splitting of the two  $S_1$  transitions, which corresponds to the coupling between spins  $S_1$  and  $S_2$ .

transitions (Figure 4.5c). This is possible if we have a microwave amplitude  $\omega_1$  that exceeds the spin-spin coupling and if there is a sufficient number of spin packets where the frequency difference between the  $S_1$  and  $S_2$  doubles strongly exceeds the spin-spin coupling. In this situation, non-selective excitation of spin  $S_2$  shifts the inversion hole on spin  $S_1$  from one of the doublet transitions to the other one. In other words, frequency of the spectral hole is changed by the spin-spin coupling.

As in the case of ELDOR-detected NMR that we discussed above, other experiments can be used for measuring the spin-spin coupling with better resolution. However, if the spin-spin coupling exceeds  $1/T_2$  of spin  $S_1$  by far, non-selective hole shifting may be more robust and more sensitive than these experiments. To the best of my knowledge, experimental proof is still missing.

### 4.3.2 Selective Hole Shifting

Selective hole shifting is the basis of the well established Davies ENDOR experiment. In this case, the excitation field  $\omega_1$  must be smaller than the hyperfine coupling  $A$  between an electron spin  $S$  and a nuclear spin  $I$  in order to selectively invert one of the two transitions of the hyperfine doublet in the EPR spectrum. This step also requires  $A > 1/T_2$ , where  $T_2$  is the transverse relaxation time of the electron spin. Figure 4.6a,b shows the effect of such an inversion pulse. You may want to draw the stick spectra of the electron and nuclear spin analogous to the spectrum shown for the case of two electron spins in Figure 4.5 (bottom).

We now consider application of a radiofrequency  $\pi$  pulse to the nuclear spin. In a situation, where  $A > 1/T_2$  for the electron spin, such a radiofrequency pulse is almost invariably transition selective. This is because the pulse amplitude in angular frequency units  $\omega_2$  is the product of the pulse amplitude in magnetic field units with the gyromagnetic

ratio, which is much smaller for nuclear spins. Without loss of generality, we assume that the radiofrequency pulse is resonant with the  $|\alpha_S\alpha_I\rangle \leftrightarrow |\alpha_S\beta_I\rangle$  transition (bold blue line in Figure 4.6b). Inversion of this transition creates nuclear spin polarization (Figure 4.6c). However, this experiment is not suited for DNP, since the first step of selective EPR hole-burning is impossible for nuclear spins that are well resolved in the NMR spectrum. Instead, the NMR spectrum can be detected on the electron spin by sweeping the radiofrequency and observing the originally burnt hole by EPR echo or FID detection. If the radiofrequency pulse is on-resonant, the original inversion hole is reduced to a saturation hole.

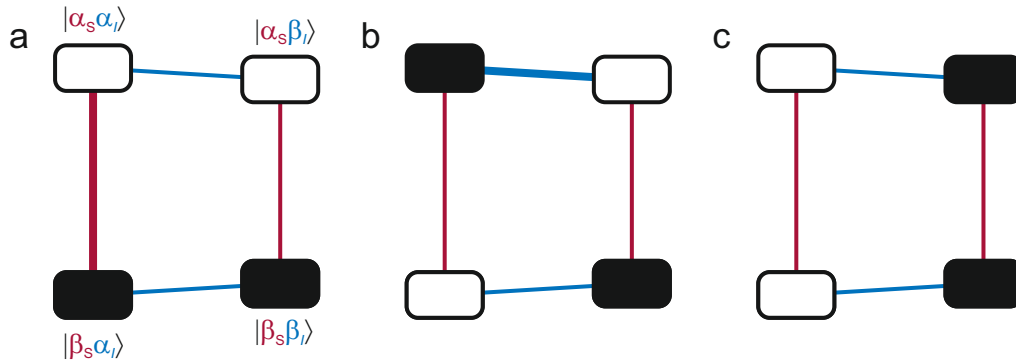


Figure 4.6: Population changes by selective hole shifting in Davies ENDOR. (a) Thermal equilibrium populations with electron-spin transitions marked red and nuclear-spin transitions marked blue. The bold red line denotes the transition where a hole is burnt. (b) Situation after electron-spin hole burning. Two-spin order is generated. The two nuclear transitions are strongly polarised, albeit with different sign. The bold blue line denotes the NMR transition that is inverted in the following step. (c) Situation after selective inversion of one NMR transition. The nuclear spin is now net polarized. Polarization on both electron spin transitions is zeroed. This corresponds to shifting half of the spectral hole depth to a side hole separated by the hyperfine splitting.

Saturation also occurs for the electron spin transition  $|\beta_S\beta_I\rangle \leftrightarrow |\alpha_S\beta_I\rangle$  that was not originally inverted. In other words, the radiofrequency pulse splits the original inversion hole into two saturation holes, one of which has a resonance offset  $A$ . By observing this side hole, one can correlate the hyperfine coupling to the NMR frequency, which is of interest if transition of different isotopes or elements occur in the same frequency range. This is generally the case at fields where the hyperfine couplings are comparable to nuclear Zeeman frequencies. Resolution in the hyperfine dimension is poor. Therefore, this experiment is rarely performed.

### 4.3.3 Shifting a Spectral Grating

The same principle as in Davies ENDOR can be applied to the spectral grating discussed in Section 4.1.2 instead to a spectral hole. The spectral grating can be conveniently detected by applying a non-selective microwave  $\pi/2$  pulse. This pulse generates a stimulated echo, which can also be considered as the FID of the grating. The radiofrequency pulse, applied between the  $\pi/2 - \tau - \pi/2$  preparation sequence and the  $\pi/2$  recall pulse, splits the grating into two subgratings, similar to splitting an inversion hole into two saturation holes. The two subgratings are shifted with respect to each other by the hyperfine coupling  $A$ . In general, this leads to destructive interference of the subgratings and thus to attenuation of the stimulated echo. This experiment is called Mims ENDOR.

The advantage of Mims ENDOR is a higher sensitivity due to utilization of more spin

packets. However, destructive interference is complete only if  $A\tau$  is an odd multiple of  $\pi$ . In the case where  $A\tau$  is an even multiple of  $\pi$ , the two subgratings superimpose constructively. The stimulated echo is then not attenuated in the limit of an infinitely broad inhomogeneous line and of ideal  $\pi/2$  pulses. In practice, some attenuation of the stimulated echo still occurs, but sensitivity is very low in this situation. Mims ENDOR thus features blind spots for hyperfine couplings  $A = 2\pi k/\tau$  with integer  $k$ . The problem can be alleviated by adding spectra measured at different interpulse delays  $\tau$  or even turned into an advantage by storing spectra at various  $\tau$  separately and performing a Fourier transformation with respect to  $\tau$ . Such a 2D Mims ENDOR experiment also correlates the hyperfine coupling to the NMR frequencies. In practice, Mims ENDOR is usually applied for small hyperfine couplings  $A < 2\pi/\tau$ . For hyperfine couplings that exceed this magnitude with the shortest possible interpulse delay  $\tau$ , given by receiver deadtime  $t_{\text{dead}}$ , Davies ENDOR is usually sufficiently sensitive and easier to perform and analyse.

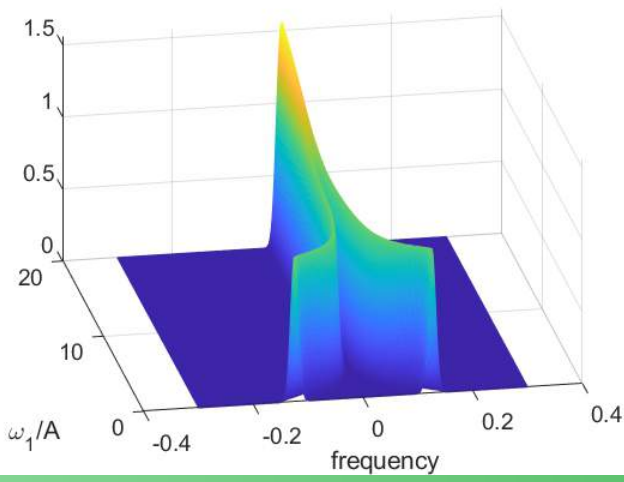


# Controlling Hyperfine Interaction

<b>5</b>	<b>Hyperfine Decoupling</b>	<b>49</b>
5.1	Secular Hyperfine Interaction	
5.2	Effect of the Pseudosecular Hyperfine Interaction	
<b>6</b>	<b>Dynamical Decoupling</b>	<b>55</b>
6.1	Phenomenological Aspects of Dynamical Decoupling	
6.2	Cluster Correlation Expansion	
6.3	Three-spin Model of Dynamical Decoupling	
	<b>Bibliography</b>	<b>61</b>
	Books	
	Articles	
	<b>Index</b>	<b>65</b>







## 5. Hyperfine Decoupling

### 5.1 Secular Hyperfine Interaction

We consider a system of an electron spin  $S = 1/2$  and a nuclear spin  $I = 1/2$  in the presence of microwave irradiation. For the moment, we truncate the hyperfine Hamiltonian to only its secular term  $A\hat{S}_z\hat{I}_z$ , which is a good approximation at very high fields where the nuclear Zeeman interaction dominates the hyperfine interaction. The total Hamiltonian in the electron-spin rotating, nuclear-spin laboratory frame is given by

$$\hat{\mathcal{H}} = \hat{\mathcal{H}}_0 + \hat{\mathcal{H}}_1 = \Omega_S\hat{S}_z + \omega_I\hat{I}_z + A\hat{S}_z\hat{I}_z + \omega_1\hat{S}_x . \quad (5.1)$$

In order to understand the effect of the microwave irradiation term  $\omega_1\hat{S}_x$  on the hyperfine term, we need to transform this Hamiltonian into its eigenbasis. As seen in Figure 5.1a,  $\hat{\mathcal{H}}$  can be separated into two  $2 \times 2$  blocks, marked blue and red, which are not connected by off-diagonal elements. Such a Hamiltonian is called block diagonal. By considering the assignment of states (kets and bras on the left side and on the top of the matrix representation), we can associate the two blocks with the  $\alpha_I$  (blue) and  $\beta_I$  (red) states of the nuclear spin. They can thus be selected by the  $\hat{I}_\alpha$  and  $\hat{I}_\beta$  projection operators.

In the product operator representation, we introduce the projection operators by the substitutions  $\hat{I}_z = \hat{I}^\alpha/2 - \hat{I}^\beta/2$  and  $\hat{1} = \hat{I}^\alpha + \hat{I}^\beta$ . We thus obtain separate spin Hamiltonians for the two blocks

$$\begin{aligned} \hat{\mathcal{H}}^\alpha &= \Omega_S\hat{S}_z + \omega_I/2 \hat{1} + A/2 \hat{S}_z + \omega_1\hat{S}_x \\ \hat{\mathcal{H}}^\beta &= \Omega_S\hat{S}_z - \omega_I/2 \hat{1} - A/2 \hat{S}_z + \omega_1\hat{S}_x . \end{aligned} \quad (5.2)$$

The terms  $\pm\omega_I/2 \hat{1}$  are not of interest for the transformation, as the unit operator  $\hat{1}$  is invariant under any rotation. The  $\hat{S}_x$  operator can be rotated to  $\hat{S}_z$  by applying a transformation  $\theta\hat{S}_y$ . We do this separately for the two subspace Hamiltonians. For the  $\hat{I}^\alpha$  subspace, we find

$$\begin{aligned} \hat{\mathcal{H}}^\alpha &\xrightarrow{\theta\hat{S}_y} \cos(\theta_\alpha) (\Omega_S + A/2) \hat{S}_z + \sin(\theta_\alpha) (\Omega_S + A/2) \hat{S}_x + \omega_I/2 \hat{1} \\ &\quad + \cos(\theta_\alpha)\omega_1\hat{S}_x - \sin(\theta_\alpha)\omega_1\hat{S}_z . \end{aligned} \quad (5.3)$$

The Hamiltonian become diagonal, if and only if the  $\hat{S}_x$  terms cancel. This leads to the condition

$$\sin(\theta_\alpha) (\Omega_S + A/2) + \cos(\theta_\alpha)\omega_1 = 0 . \quad (5.4)$$

By solving for  $\theta_\alpha$  we obtain

$$\theta_\alpha = \arctan \frac{-\omega_1}{\Omega_S + A/2} . \quad (5.5)$$

The analogous steps for the  $\hat{I}^\beta$  subspace yield

$$\theta_\beta = \arctan \frac{-\omega_1}{\Omega_S - A/2} . \quad (5.6)$$

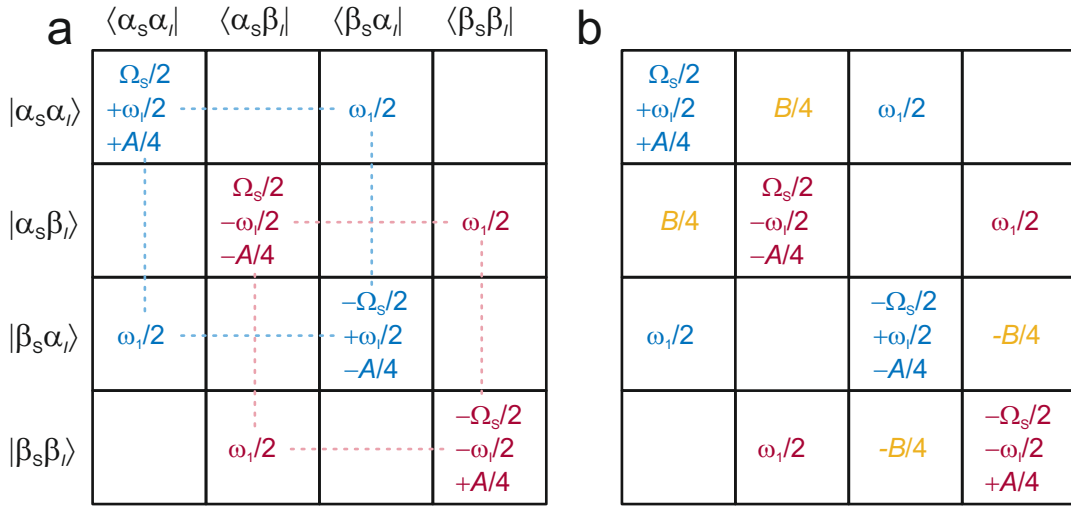


Figure 5.1: Matrix representation of the spin Hamiltonian for an  $S = 1/2, I = 1/2$  system with electron spin resonance offset  $\Omega_S \hat{S}_z$ , and nuclear Zeeman interaction  $\omega_I \hat{I}_z$  during microwave irradiation  $\omega_1 \hat{S}_x$ . (a) Only secular hyperfine coupling  $A \hat{S}_z \hat{I}_z$  is considered. The Hamiltonian is block-diagonal with the two blocks indicated by dashed light blue ( $\hat{I}^\alpha$  manifold) and dashed light red ( $\hat{I}^\beta$  manifold) lines. (b) Pseudo-secular coupling  $B \hat{S}_z \hat{I}_x$  is also considered. The Hamiltonian is no longer block-diagonal.

Using  $\sin^2 \theta + \cos^2 \theta = 1$ , we can identify

$$\begin{aligned} \cos \theta_\alpha &= \frac{\Omega_S + A/2}{\sqrt{(\Omega_S + A/2)^2 + \omega_1^2}} = \frac{\Omega_S + A/2}{\omega_{\text{eff}}^\alpha} \\ \sin \theta_\alpha &= \frac{-\omega_1}{\sqrt{(\Omega_S + A/2)^2 + \omega_1^2}} = \frac{-\omega_1}{\omega_{\text{eff}}^\alpha} . \end{aligned} \quad (5.7)$$

We insert these values into Eq. (5.3) and obtain

$$\begin{aligned} \hat{\mathcal{H}}_{\text{EB}}^\alpha &= \frac{(\Omega_S + A/2)^2}{\omega_{\text{eff}}^\alpha} \hat{S}_z + \omega_I/2 \hat{\mathbb{1}} + \frac{\omega_1^2}{\omega_{\text{eff}}^\alpha} \omega_1 \hat{S}_z \\ &= \frac{(\Omega_S + A/2)^2 + \omega_1^2}{\omega_{\text{eff}}^\alpha} \hat{S}_z + \omega_I/2 \hat{\mathbb{1}} \\ &= \omega_{\text{eff}}^\alpha \hat{S}_z + \omega_I/2 \hat{\mathbb{1}} . \end{aligned} \quad (5.8)$$

Analogously, we find for the  $\hat{I}^\beta$  subspace

$$\hat{\mathcal{H}}_{\text{EB}}^\beta = \omega_{\text{eff}}^\beta \hat{S}_z + \omega_I/2 \hat{\mathbb{1}} . \quad (5.9)$$

The longish derivation confirms the expectation that, in each subspace, we rotated the effective field towards the new  $z$  axis. This effective field can be computed by vector addition of the two components along  $z$  and  $x$  in the original frame. Likewise,  $\theta_\alpha$  and  $\theta_\beta$  can be inferred easily from a vector picture, as we did it for  $\eta_\alpha$  and  $\eta_\beta$  in the basic magnetic resonance course. Using the formal product operator computations, as we did here, is convenient when deriving expressions with programs like Mathematica, as it may save us from explicitly picturing all rotations.

We are now in a position to combine the two subspace Hamiltonians to the total Hamiltonian

$$\begin{aligned} \hat{\mathcal{H}}_{\text{EB}} &= \hat{I}^\alpha \hat{\mathcal{H}}_{\text{EB}}^\alpha + \hat{I}^\beta \hat{\mathcal{H}}_{\text{EB}}^\beta \\ &= \frac{\omega_{\text{eff}}^\alpha + \omega_{\text{eff}}^\beta}{2} \hat{S}_z + \omega_I \hat{I}_z + \left( \omega_{\text{eff}}^\alpha - \omega_{\text{eff}}^\beta \right) \hat{S}_z \hat{I}_z . \end{aligned} \quad (5.10)$$

We find that the hyperfine coupling is reduced from  $A$  to  $\left( \omega_{\text{eff}}^\alpha - \omega_{\text{eff}}^\beta \right)$ .

This is still a complicated result, because the residual hyperfine coupling depends on the ratios between three quantities, the resonance offset  $\Omega_S$ , the microwave field amplitude  $\omega_1$ , and the unperturbed hyperfine coupling  $A$ . We first discuss the two limiting cases with respect to resonance offset. On resonance ( $\Omega_S = 0$ ), we find  $\omega_{\text{eff}}^\alpha = \omega_{\text{eff}}^\beta = \sqrt{A^2/4 + \omega_1^2}$ . Hence,

$$\lim_{\Omega_S \rightarrow 0} \omega_{\text{eff}}^\alpha - \omega_{\text{eff}}^\beta = 0 . \quad (5.11)$$

For on-resonant spin packets hyperfine decoupling is perfect even at very small microwave field amplitudes  $\omega_1$ . For  $\Omega_S \rightarrow \infty$ , we can neglect  $\omega_1^2$  in the expressions for  $\omega_{\text{eff}}^{\alpha/\beta}$  with respect to  $(\Omega_S \pm A/2)^2$ . It follows that

$$\lim_{\Omega_S \rightarrow \infty} \omega_{\text{eff}}^\alpha - \omega_{\text{eff}}^\beta = A . \quad (5.12)$$

For  $\Omega_S \gg \omega_1$ , the hyperfine coupling remains practically unperturbed.

The transition between the two limits is most easily assessed by plotting the ratio between the residual coupling  $\omega_{\text{eff}}^\alpha - \omega_{\text{eff}}^\beta$  and the unperturbed coupling  $A$  versus the ratio between the microwave field amplitude  $\omega_1$  and the resonance offset  $\Omega_S$ . As the result also depends on the ratio between  $\omega_1$  and  $A$ , the plot is two-dimensional. We represent  $(\omega_{\text{eff}}^\alpha - \omega_{\text{eff}}^\beta)/A$  as a decadic logarithm (Figure 5.2). Efficient decoupling in this simple experiment requires that the microwave field amplitude  $\omega_1$  exceeds the resonance offset  $\Omega_S$  by far. For  $\omega_1 \approx \Omega_S$  decoupling is poor even if  $\omega_1$  is much larger than the unperturbed hyperfine coupling  $A$ . For observation of nuclear frequencies via the electron spin, this problem can be compensated by an observer sequence that limits the resonance offset of spin packets that contribute to the signal. The easiest way of doing so is by using a spin-locked echo sequence  $\pi/2 - \tau - \text{HTA} = \tau - \text{echo}$ , where HTA denotes a high-turning angle pulse with the maximum available microwave field amplitude  $\omega_{1,\text{max}}$ . The amplitude or even the waveform of the  $\pi/2$  pulse can then be adjusted in a way that guarantees  $\Omega_S \ll \omega_{1,\text{max}}$  for all spin packets that strongly contribute to the observer echo. There are two ways for observing the hyperfine-decoupled NMR spectrum via the electron spin [JS97]. First, radiofrequency can be irradiated during the HTA pulse. If the frequency matches a

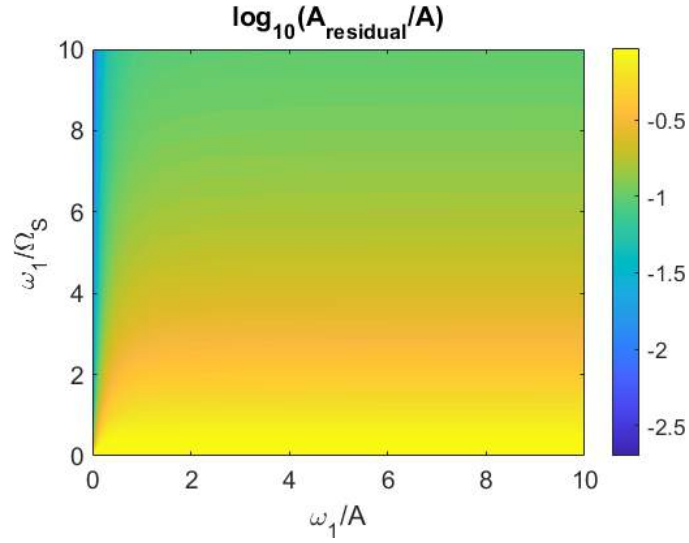


Figure 5.2: Hyperfine decoupling efficiency  $\log_{10} \left[ (\omega_{\text{eff}}^{\alpha} - \omega_{\text{eff}}^{\beta})/A \right]$  as a function of the ratios between microwave field amplitude  $\omega_1$  and unperturbed hyperfine coupling  $A$  (horizontal) as well as between  $\omega_1$  and resonance offset  $\Omega_S$  (vertical).

decoupled nuclear spin transition, the spin-locked echo is attenuated (hyperfine-decoupled ENDOR). Second, the length of the HTA pulse can be varied. This hyperfine-decoupled ESEEM experiment depends on generation of nuclear coherence, which in turn requires a substantial pseudo-secular contribution  $B\hat{S}_z\hat{I}_x$  of the hyperfine coupling. In the following Section, we consider the behaviour of this term under hyperfine decoupling.

## 5.2 Effect of the Pseudosecular Hyperfine Interaction

The pseudo-secular hyperfine coupling term  $B\hat{S}_z\hat{I}_x$  introduces off-diagonal elements that mix the  $\hat{I}^{\alpha}$  and  $\hat{I}^{\beta}$  subspaces (Figure 5.1b). Thus, the Hamiltonian is no longer block-diagonal and cannot be transformed to its eigenbasis by the procedure discussed in Section 5.1. In principle, any  $4 \times 4$  Hamiltonian matrix can be analytically diagonalized. However, the resulting expressions are too complicated for being of practical use. Therefore, we first apply the transformation discussed above to the pseudo-secular term and discuss the result.

We start by observing that

$$\theta_{\alpha}\hat{S}_y\hat{I}^{\alpha} + \theta_{\beta}\hat{S}_y\hat{I}^{\beta} = \frac{\theta_{\alpha} + \theta_{\beta}}{2}\hat{S}_y + \frac{\theta_{\alpha} - \theta_{\beta}}{2}2\hat{S}_y\hat{I}_z = \theta_{+}\hat{S}_y + \theta_{-}2\hat{S}_y\hat{I}_z \quad (5.13)$$

Of the two Cartesian product operator terms,  $2\hat{S}_y\hat{I}_z$  commutes with  $\hat{S}_z\hat{I}_x$ . Thus, we find for the pseudo-secular term in the eigenbasis of the secular part of the spin Hamiltonian

$$B\hat{S}_z\hat{I}_x \xrightarrow{\theta_{+}\hat{S}_y} \cos(\theta_{+})B\hat{S}_z\hat{I}_x + \sin(\theta_{+})B\hat{S}_x\hat{I}_x. \quad (5.14)$$

The term with factor  $\cos(\theta_{+})$  can be treated as shown in the basic magnetic resonance lecture. Hence, the transformation  $\hat{T}_{\text{psec}} = \xi'\hat{I}_y + \eta'2\hat{S}_z\hat{I}_y$  removes this term. The angles  $\xi'$  and  $\eta'$  can be computed in analogy to  $\xi$  and  $\eta$  in the absence of decoupling by replacing  $A$  by  $(\omega_{\text{eff}}^{\alpha} - \omega_{\text{eff}}^{\beta})$  and  $B$  by  $\cos(\theta_{+})B$ . This transformation also provides the (partially) hyperfine-decoupled nuclear frequencies  $\omega'_{\alpha}$  and  $\omega'_{\beta}$  for substantial pseudo-secular hyperfine coupling, disregarding for the moment the term  $\sin(\theta_{+})B\hat{S}_x\hat{I}_x$ . We now transform this term

to the frame that includes the effects of, both, the microwave irradiation and the remaining part of the pseudo-secular hyperfine coupling

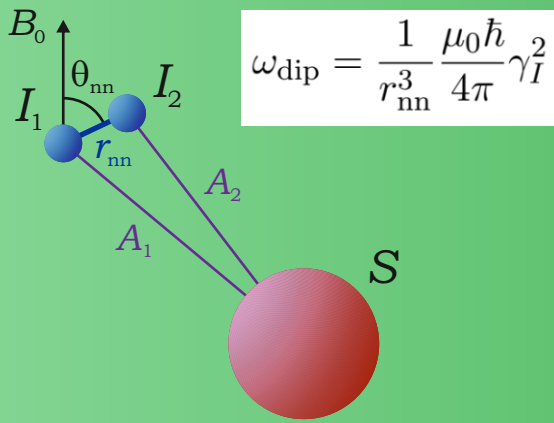
$$\sin(\theta_+)B\hat{S}_x\hat{I}_x \xrightarrow{\xi'\hat{I}_y} \cos(\xi')B\hat{S}_x\hat{I}_x - \sin(\xi')B\hat{S}_x\hat{I}_z . \quad (5.15)$$

We have made use of the fact that  $\hat{S}_x\hat{I}_x$  commutes with  $\hat{S}_z\hat{I}_y$ .

Of the remaining two terms,  $\hat{S}_x\hat{I}_z$  connects levels that differ in their electron spin magnetic quantum number  $m_S$  and agree in their nuclear spin magnetic quantum number  $m_I$ . Such levels are split by at least  $\omega_1$ . If we define hyperfine decoupling as a situation where the microwave field is much larger than the pseudo-secular coupling  $B$ , this term can be neglected irrespective of the magnitude of other interactions. The same does not apply to the term  $\cos(\xi')B\hat{S}_x\hat{I}_x$ , which acts on electron-nuclear zero- and double-quantum transitions. Among these, the zero-quantum transition has a frequency of roughly  $|\sqrt{\Omega_S^2 + \omega_1^2} - |\omega_I||$ . If this frequency tends to zero, the off-diagonal element  $\cos(\xi')B\hat{S}_x\hat{I}_x$  causes additional mixing of levels. For on-resonant spin packets ( $\Omega_S = 0$ ), such mixing occurs at the NOVEL DNP condition  $\omega_1 \approx |\omega_I|$ .

The same situation can be treated by other sequences of transformations [JS96]. The general approach is to apply simple transformations and analyse the remaining off-diagonal terms for their significance. If the levels connected by an off-diagonal term are split by a frequency much larger than the term itself, then this term can be safely neglected. A series of simple transformations can thus lead to an analytical solution that is a good approximation.





## 6. Dynamical Decoupling

*In the low-temperature limit, electron spin decoherence is driven by interaction with the nuclear spin bath. Such decoherence can be suppressed by dynamical decoupling, a term that refers to multiple refocusing of the coherence, for instance, by the Carr-Purcell sequence. We briefly cluster correlation expansion, which has been used for simplifying the problem of an infinite coupled network of nuclear spins. Cluster correlation up to cluster size 2 corresponds to describing the coherence decay as a product of echo modulation functions of three-spin systems that consist of the electron spin and two nuclear spins. We discuss a simple analytical treatment of this three-spin system and derive an expression for echo modulation by product operator formalism.*

### 6.1 Phenomenological Aspects of Dynamical Decoupling

Decay kinetics of the Hahn echo of dilute electron spins attains a low-temperature limit near 50 K for organic radicals and near 10 K for transition metal ions with spin 1/2. In most samples, decay does not conform to first-order kinetics in this regime, i.e., it is not described by a single exponential. Instead, this decay can be modelled by a stretched exponential function,  $V(\tau) = \exp[-(2\tau/T_m)^\xi]$ , where  $2\tau$  is the total length of the Hahn echo with interpulse delay  $\tau$  and  $T_m$  the phase memory time. Precise measurements show that in many cases a sum of two stretched exponentials is required for such modeling [Soe+18; Soe+21]. Echo decay with  $\xi = 2$  is expected for diffusive processes, such as nuclear spin diffusion, and can be suppressed by Carr-Purcell multiple refocusing [HEE03]. Experimental results for a bulky nitroxide radical in a glassy water:glycerol matrix (1:1 v/v) are shown in Figure 6.1. On the simplest level, the effect can be understood by observing that

$$\exp[-(Nt/T_m)^\xi] < \exp[-(t/T_m)^\xi]^N \quad (\text{for } \xi > 1) \quad . \quad (6.1)$$

Because the number of nuclear spins coupled to the electron spin and among themselves is very large, the problem is usually treated by a spin-bath approach. Excitation of the electron spin changes the hyperfine fields at the nuclei, thus disturbing equilibrium of the

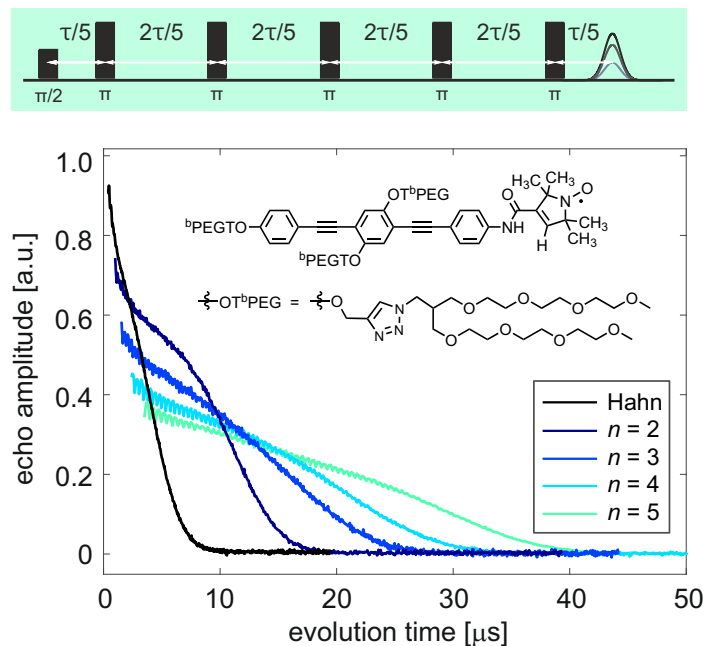


Figure 6.1: Prolongation of electron spin decoherence time by dynamical decoupling for a nitroxide radical (inset) in water:glycerol 1:1 v/v. The plot shows the Hahn echo decay (black) and decays of the final echo after Carr-Purcell sequences with  $n = 2 \dots 5$  refocusing pulses. The pulse sequence at the top is the Carr-Purcell experiment with  $n = 5$  and a total time  $2\tau$ . Adapted from [Soe+21].

nuclear spin bath. Dipole-dipole coupling between nuclear spins then causes magnetization exchange between nuclei. This requires that nuclear-nuclear coupling is of the same order of magnitude as the difference between their hyperfine couplings. The resulting backaction on the electron spin was historically considered as a fluctuating hyperfine field due to the spin bath at the electron spin. Such fluctuating fields lead to stochastic defocusing of coherence and thus to coherence loss (decoherence). An early quantitative treatment by Milov *et al.* provided  $\xi = 7/4$ .

## 6.2 Cluster Correlation Expansion

The problem of nuclear spin-diffusion driven electron spin decoherence attracted new interest in the context of quantum information processing. Witzel and Das Sarma realized that the inhomogeneous spatial distribution of nuclear spins simplifies the problem [WS07]. Couplings between nuclei need to be considered only within disjoint sets of nuclei (clusters), but not between such sets. For instance, the proton-proton distance in a water molecule is 1.51 Å, whereas the hydrogen-bond distance to the oxygen atom in a neighbouring water molecule is 2.8 Å. Dipole-dipole couplings between protons in different water molecules are thus much smaller than those within water molecules. As suggested by this consideration, it has been found by numerical computations that a correlated cluster expansion up to order two (pairs of protons) provides reasonable predictions for nitroxide and trityl radicals in glassy frozen water:glycerol mixtures, even though the predictions were made on the basis of molecular dynamics simulations for pure water [CJS20].

To a first approximation, contributions of individual clusters to the logarithm  $\ln V(t)$  of the decoherence function add [WS07] because contributions to the decay function  $V(t)$



multiply. Hence, we should be able to understand the basics of dynamical decoupling by considering spin dynamics of a system consisting of one electron spin and two nuclear spins.

## 6.3 Three-spin Model of Dynamical Decoupling

### 6.3.1 Defining a Minimal System

It is useful to distinguish between numerical spin dynamics simulations that aim at quantitative prediction for an experimentally accessible system and computations that aim at understanding the physics of a phenomenon. In the latter case, it is useful to work with the minimal system that reproduces the phenomenon. Later on, one can still study how the outcome changes for more realistic assumptions on the Hamiltonian and interaction parameters.

In the case at hand, we know that nuclear spin-diffusion driven decoherence depends on homonuclear dipole-dipole coupling. The nuclear spin part of the Hamiltonian is thus given by

$$\hat{\mathcal{H}}_{\text{nuc}} = \omega_I \left( \hat{I}_{1,z} + \hat{I}_{2,z} \right) + \omega_{\text{dip}} \left( 1 - 3 \cos^2 \theta_{\text{nn}} \right) \left[ \hat{I}_{1,z} \hat{I}_{2,z} - \frac{1}{4} \left( \hat{I}_1^+ \hat{I}_2^- + \hat{I}_1^- \hat{I}_2^+ \right) \right], \quad (6.2)$$

where  $\theta_{\text{nn}}$  is the angle between the static magnetic field  $B_0$  and the nuclear-nuclear vector and the dipole-dipole coupling  $\omega_{\text{dip}}$  is

$$\omega_{\text{dip}} = \frac{1}{r_{\text{nn}}^3} \frac{\mu_0 \hbar}{4\pi} \gamma_I^2 \quad (6.3)$$

with the internuclear distance  $r_{\text{nn}}$ . We have neglected chemical shift, which is much smaller than nuclear dipole-dipole coupling within clusters and much smaller than hyperfine couplings that can lead to decoherence on the time scale of electron spin echo experiments. For the same reason, we can neglect J coupling in the nuclear spin pair.

If the two nuclear spins have the same hyperfine coupling, they are magnetically equivalent and back action of nuclear flip-flops on the electron spin is suppressed. Hence, we need to assume a difference in hyperfine coupling to the electron spin between the two nuclear spins,

$$\hat{\mathcal{H}}_{\text{hfi}} = A_1 \hat{S}_z \hat{I}_{1,z} + A_2 \hat{S}_z \hat{I}_{2,z}, \quad (6.4)$$

with  $A_1 \neq A_2$ . When considering evolution of coherence during a block  $\tau - (\pi)_x - \tau$ , we can set the resonance offset  $\Omega_S$  of the electron spin to zero as it is refocused by the  $\pi$  pulse. Although the pseudo-secular hyperfine coupling  $B_1 \hat{S}_z \hat{I}_{1,x} + B_2 \hat{S}_z \hat{I}_{2,x}$  may be significant, we neglect it for our analytical treatment, because the effect under consideration does not require this pseudo-secular coupling.

### 6.3.2 Product Operator Formalism for the Refocusing Block

Without losing generality, we can consider evolution of electron spin coherence  $\hat{S}_x$  (zero phase) during a refocusing block of total duration  $T = 2\tau$ . In product operator formalism, this is written as

$$\hat{S}_x \xrightarrow{\hat{\mathcal{H}}_0 \tau} \xrightarrow{\pi \hat{S}_x} \xrightarrow{\hat{\mathcal{H}}_0 \tau} \dots, \quad (6.5)$$

where  $\hat{\mathcal{H}}_0 = \hat{\mathcal{H}}_{\text{hfi}} + \hat{\mathcal{H}}_{\text{nuc}}$ . However, product operator formalism cannot be applied without precautions, since the two terms of  $\hat{\mathcal{H}}_{\text{nuc}}$  do not commute.

The off-diagonal flip-flop term of  $\hat{\mathcal{H}}_{\text{nuc}}$  with operator  $\hat{I}_1^+ \hat{I}_2^- + \hat{I}_1^- \hat{I}_2^+ = 2(\hat{I}_{1,x} \hat{I}_{2,x} + \hat{I}_{1,y} \hat{I}_{2,y})$  connects two pairs of levels. These are the pairs  $(\hat{S}^\alpha \hat{I}_1^\alpha \hat{I}_2^\beta, \hat{S}^\alpha \hat{I}_1^\beta \hat{I}_2^\alpha)$  with secular splitting  $(A_1 - A_2)/2$  and  $(\hat{S}^\beta \hat{I}_1^\alpha \hat{I}_2^\beta, \hat{S}^\beta \hat{I}_1^\beta \hat{I}_2^\alpha)$  with secular splitting  $(A_2 - A_1)/2$ . Accordingly, the Hamiltonian can be diagonalized by the transformation

$$\hat{\mathcal{H}} \xrightarrow{\eta \hat{T}_{\text{EB}}} \hat{\mathcal{H}}_{\text{EB}} \quad (6.6)$$

with the rotation angle

$$\eta = \arctan \frac{\omega_{\text{nn}}}{A_1 - A_2} \quad (6.7)$$

with  $\omega_{\text{nn}} = \omega_{\text{dip}} (1 - 3 \cos^2 \theta_{\text{nn}})$  where the arctan function is understood as four quadrant inverse tangent. The state-space rotation is effected by the operator

$$\hat{T}_{\text{EB}} = 2\hat{S}_z \hat{I}_{1,y} \hat{I}_{2,x} - 2\hat{S}_z \hat{I}_{1,x} \hat{I}_{2,y} \quad (6.8)$$

With the nuclear zero-quantum splitting of the level pairs in the eigenbasis,

$$\omega_{\text{nZQ}} = \frac{1}{2} \sqrt{(A_1 - A_2)^2 + \omega_{\text{nn}}^2}, \quad (6.9)$$

the Hamiltonian in its eigenbasis becomes

$$\hat{\mathcal{H}}_{\text{EB}} = \omega_I (\hat{I}_{1,z} + \hat{I}_{2,z}) + \omega_{\text{nn}} \hat{I}_{1,z} \hat{I}_{2,z} + A'_1 \hat{S}_z \hat{I}_{1,z} + A'_2 \hat{S}_z \hat{I}_{2,z}, \quad (6.10)$$

where

$$A'_{1,2} = \frac{A_1 + A_2}{2} \pm \omega_{\text{nZQ}}. \quad (6.11)$$

Hence, the product operator expression  $\hat{\rho}(\tau)$  after one refocusing block can be computed as

$$\hat{S}_x \xrightarrow{\eta \hat{T}_{\text{EB}}} \hat{\mathcal{H}}_{\text{EB}} \tau \xrightarrow{-\eta \hat{T}_{\text{EB}}} \pi \hat{S}_x \xrightarrow{\eta \hat{T}_{\text{EB}}} \hat{\mathcal{H}}_{\text{EB}} \tau \xrightarrow{-\eta \hat{T}_{\text{EB}}} \hat{\rho}(2\tau). \quad (6.12)$$

In  $\hat{\rho}(2\tau)$ , we can neglect all product operator terms that do not correspond to electron coherence  $\hat{S}_x$  or  $\hat{S}_y$ . After a lengthy product operator computation,<sup>1</sup> we find that  $\langle \hat{S}_y \rangle(2\tau) = 0$  and

$$\langle \hat{S}_x \rangle(2\tau) = 1 - \sin^2 \eta \cos^2 \eta \left[ \frac{3}{2} - 2 \cos(\omega_{\text{nZQ}} \tau) + \frac{1}{2} \cos(2\omega_{\text{nZQ}} \tau) \right]. \quad (6.13)$$

Using Eq. (6.7), we further obtain a modulation depth factor

$$\lambda = \sin^2 \eta \cos^2 \eta = \frac{(A_1 - A_2)^2 \omega_{\text{nn}}^2}{\left[ (A_1 - A_2)^2 + \omega_{\text{nn}}^2 \right]^2}. \quad (6.14)$$

The coherence loss term is proportional to the modulation depth factor and thus approaches zero if  $A_1 - A_2 \gg \omega_{\text{nn}}$ . This applies to nuclear pairs very close to the electron spin. Modulation depth also approaches zero for  $A_1 - A_2 \ll \omega_{\text{nn}}$ , which applies to nuclear pairs very far from the electron spin. In the three-spin system, coherence completely

<sup>1</sup>The Mathematica package `Spinop_guje.wl` and the Mathematica notebook `dyndec_three_spin.nb` in the course Moodle demonstrate this

recurs at  $\tau = 2\pi/\omega_{nZQ}$ . However, if the electron spin is coupled to many spin pairs,  $\omega_{nZQ}$  is distributed due to the orientation dependence of  $\omega_{nm}$  and the dependence of  $A_1 - A_2$  on electron-nuclear distance and orientation of the electron-nuclear vectors. Destructive interference then leads to coherence loss with increasing time  $T$ .

Further, the modulations due to the various nuclear spin pairs combine multiplicatively. If we index these pairs by  $j$  and define the unmodulated fraction  $f_{u,j}$  for a single nuclear spin pair, then the unmodulated fraction after considering all pairs is  $\prod_j f_{u,j}$ . Since all the  $f_{u,j}$  are smaller than unity and the number of contributing nuclear spin pairs is huge, the total unmodulated fraction tends to zero. This consideration also shows that electron decoherence will be incomplete if the number of nuclear spin pairs is small, as can happen for a protonated molecule in a deuterated matrix on time scales where decoherence due to deuteron pairs is still negligible.

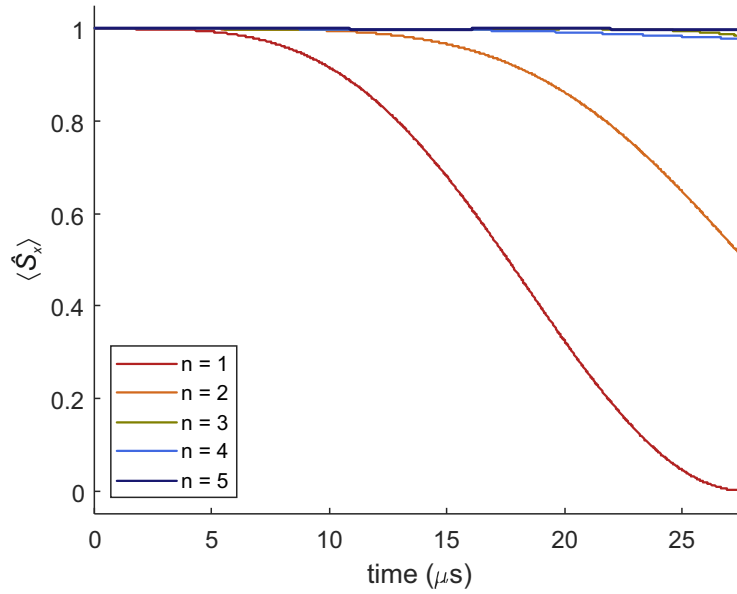


Figure 6.2: Principle of dynamical decoupling illustrated on a three-spin system consisting of an electron spin  $S = 1/2$  and two protons  $I_1 = I_2 = 1/2$ . A proton-proton distance of  $1.51 \text{ \AA}$  and an angle between the proton-proton vector and the static magnetic field of  $25^\circ$  were assumed. The difference between the hyperfine couplings  $A_1$  and  $A_2$  of the two protons was matched to their dipole-dipole interaction  $\omega_{nm}$ . The maximum time corresponds to  $2\pi/\omega_{nZQ}$ , where electron coherence is lost completely with a single refocusing pulse ( $n = 1$ ). For an increasing number of refocusing pulses, coherence loss reduces at the same total evolution time.

Dynamical decoupling can now be understood from the  $\tau$ -dependence of  $\langle \hat{S}_x \rangle(2\tau)$  in Eq (6.13). As long as  $2\omega_{nZQ}\tau$  is very small, the cosine factors can be approximated by  $1 - x_i^2/2$  with  $x_1 = \omega_{nZQ}\tau$  and  $x_2 = \omega_{nZQ}\tau$ . Now consider the replacement of a single block with interpulse delay  $\tau$  by two blocks with interpulse delays  $\tau/2$ . In the latter case, the remaining coherence is

$$\left[1 - \frac{(x/2)^2}{2}\right]^2 = 1 - \frac{x^2}{4} + \frac{x^4}{64} > 1 - \frac{x^2}{2}. \quad (6.15)$$

For nuclear spin pairs that contribute to decoherence of the electron spin,  $\omega_{nZQ}$  cannot be much larger than  $\omega_{\text{dip}}$ , as defined in Eq. (6.3). Otherwise,  $A_1 - A_2$  would need to be much larger than  $\omega_{\text{dip}}$ , which would imply vanishing modulation depth  $\sin^2 \eta \cos^2 \eta$ . Hence,

the upper limit of the interpulse delay, where dynamical decoupling is still efficient, is  $\tau_{\max} \approx 2\pi/\omega_{\text{dip}}$ . When  $\tau$  is reduced below that value by inserting additional  $\pi$  refocusing pulses, decoherence slows down.

This is illustrated in Fig. 6.2. We assume a proton-proton distance as in water and an arbitrary angle between the proton-proton vector and the magnetic field ( $25^\circ$ ). In order to see the maximum effect, we matched the difference of the two hyperfine couplings to  $\omega_{\text{nn}}$ . We set the maximum observation time to  $T_{\max} = 2\pi/\omega_{\text{nZQ}}$ . Since for one refocusing pulse, the evolution time is  $\tau = T/2$ , this corresponds to maximum coherence loss and, because we have matched the two interactions, to complete loss of electron coherence. If we increase the number  $n$  of refocusing pulses, coherence decays more slowly. In the case at hand,  $n \geq 3$  suffices to avoid strong coherence loss up to  $T_{\max}$ .

Finally, we can ask the question where the lost coherence ends up. Analysis of the complete product operator expression at time  $2\tau$  reveals that electron-nuclear-nuclear triple-quantum coherence  $\hat{S}_y\hat{I}_{1y}\hat{I}_{2,x} - \hat{S}_y\hat{I}_{1x}\hat{I}_{2,y}$ , electron spin coherence in single nuclear spin antiphase  $\hat{S}_y\hat{I}_{1z} - \hat{S}_y\hat{I}_{2z}$  and electron spin coherence in double nuclear spin antiphase  $\hat{S}_x\hat{I}_{1z}\hat{I}_{2z}$  are generated. Hence, no net nuclear polarization is generated, not even if another  $\pi/2$  pulse is applied to the electron spin at the time of refocusing. The experiment  $(\pi/2)_{S,x} - \tau - (\pi)_{S,x} - \tau - (\pi/2)_{S,x}$  generates electron-nuclear two-spin order with different sign on the two nuclear spins.

## Principles of pulse electron paramagnetic resonance

Arthur Schweiger and Gunnar Jeschke

# Literature

## Books

- [Lev08] Malcolm Levitt. *Spin Dynamics: Basics of Nuclear Magnetic Resonance*. 1st edition. Chichester: John Wiley & Sons, 2008 (cited on pages 7, 8, 12).
- [Pri18] Stephan Pribitzer. *New Methods in Pulse Electron Paramagnetic Resonance with Frequency-Swept Pulses*. 1st edition. ETH Zürich: Diss. ETH No. 25604, 2018 (cited on page 18).
- [SJ01] Arthur Schweiger and Gunnar Jeschke. *Principles of Pulse Electron Paramagnetic Resonance*. 1st edition. Oxford: Oxford University Press, 2001 (cited on pages 7, 8, 12, 17).

## Articles

- [Bri16] Andreas Brinkmann. “Introduction to average Hamiltonian theory. I. Basics”. In: *Concepts in Magnetic Resonance Part A* 45A.6 (2016), e21414. DOI: <https://doi.org/10.1002/cmr.a.21414>. eprint: <https://onlinelibrary.wiley.com/doi/pdf/10.1002/cmr.a.21414>. URL: <https://onlinelibrary.wiley.com/doi/abs/10.1002/cmr.a.21414> (cited on page 24).
- [CJS20] Elizabeth R. Canarie, Samuel M. Jahn, and Stefan Stoll. “Quantitative Structure-Based Prediction of Electron Spin Decoherence in Organic Radicals”. In: *The Journal of Physical Chemistry Letters* 11.9 (2020). PMID: 32282218, pages 3396–3400. DOI: [10.1021/acs.jpcclett.0c00768](https://doi.org/10.1021/acs.jpcclett.0c00768). eprint: <https://doi.org/10.1021/acs.jpcclett.0c00768>. URL: <https://doi.org/10.1021/acs.jpcclett.0c00768> (cited on page 56).
- [CSS02] Kristin E. Cano, Mari A. Smith, and A.J. Shaka. “Adjustable, Broadband, Selective Excitation with Uniform Phase”. In: *Journal of Magnetic Resonance* 155.1 (2002), pages 131–139. ISSN: 1090-7807. DOI: <https://doi.org/10.1006/>

- jmre.2002.2506. URL: <https://www.sciencedirect.com/science/article/pii/S1090780702925061> (cited on page 32).
- [DJ17] Andrin Doll and Gunnar Jeschke. “Wideband frequency-swept excitation in pulsed EPR spectroscopy”. In: *Journal of Magnetic Resonance* 280 (2017). Special Issue on Methodological advances in EPR spectroscopy and imaging, pages 46–62. ISSN: 1090-7807. DOI: <https://doi.org/10.1016/j.jmr.2017.01.004>. URL: <https://www.sciencedirect.com/science/article/pii/S1090780717300046> (cited on pages 25, 28, 30–33, 35).
- [Haa+94] J. Haase et al. “Population Transfers for NMR of Quadrupolar Spins in Solids”. In: *Journal of Magnetic Resonance, Series A* 109.1 (1994), pages 90–97. ISSN: 1064-1858. DOI: <https://doi.org/10.1006/jmra.1994.1138>. URL: <https://www.sciencedirect.com/science/article/pii/S1064185884711387> (cited on page 35).
- [HEE03] James R Harbridge, Sandra S Eaton, and Gareth R Eaton. “Comparison of electron spin relaxation times measured by Carr–Purcell–Meiboom–Gill and two-pulse spin-echo sequences”. In: *Journal of Magnetic Resonance* 164.1 (2003), pages 44–53. ISSN: 1090-7807. DOI: [https://doi.org/10.1016/S1090-7807\(03\)00182-4](https://doi.org/10.1016/S1090-7807(03)00182-4). URL: <https://www.sciencedirect.com/science/article/pii/S1090780703001824> (cited on page 55).
- [JS96] Gunnar Jeschke and Arthur Schweiger. “Generation and transfer of coherence in electron-nuclear spin systems by non-ideal microwave pulses”. In: *Molecular Physics* 88.2 (1996), pages 355–383. DOI: [10.1080/00268979650026398](https://doi.org/10.1080/00268979650026398). eprint: <https://doi.org/10.1080/00268979650026398>. URL: <https://doi.org/10.1080/00268979650026398> (cited on page 53).
- [JS97] Gunnar Jeschke and Arthur Schweiger. “Hyperfine decoupling in electron spin resonance”. In: *The Journal of Chemical Physics* 106.24 (1997), pages 9979–9991. DOI: [10.1063/1.474073](https://doi.org/10.1063/1.474073). eprint: <https://doi.org/10.1063/1.474073>. URL: <https://doi.org/10.1063/1.474073> (cited on page 51).
- [PDJ16] Stephan Pribitzer, Andrin Doll, and Gunnar Jeschke. “SPIDYAN, a MATLAB library for simulating pulse EPR experiments with arbitrary waveform excitation”. In: *Journal of Magnetic Resonance* 263 (2016), pages 45–54. ISSN: 1090-7807. DOI: <https://doi.org/10.1016/j.jmr.2015.12.014>. URL: <https://www.sciencedirect.com/science/article/pii/S1090780715003158> (cited on page 8).
- [RSB91] Muppurala Ravikumar, Rajesh Shukla, and Aksel A. Bothner-By. “Relaxation and dynamics of coupled spin systems subjected to continuous radio frequency fields”. In: *The Journal of Chemical Physics* 95.5 (1991), pages 3092–3098. DOI: [10.1063/1.460866](https://doi.org/10.1063/1.460866). eprint: <https://doi.org/10.1063/1.460866>. URL: <https://doi.org/10.1063/1.460866> (cited on page 18).
- [Soe+18] Janne Soetbeer et al. “Dynamical decoupling of nitroxides in o-terphenyl: a study of temperature, deuteration and concentration effects”. In: *Phys. Chem. Chem. Phys.* 20 (3 2018), pages 1615–1628. DOI: [10.1039/C7CP07074H](https://doi.org/10.1039/C7CP07074H). URL: <http://dx.doi.org/10.1039/C7CP07074H> (cited on page 55).
- [Soe+21] Janne Soetbeer et al. “Dynamical decoupling in water–glycerol glasses: a comparison of nitroxides, trityl radicals and gadolinium complexes”. In: *Phys. Chem. Chem. Phys.* 23 (9 2021), pages 5352–5369. DOI: [10.1039/D1CP00055A](https://doi.org/10.1039/D1CP00055A). URL: <http://dx.doi.org/10.1039/D1CP00055A> (cited on pages 55, 56).

- [SS06] Stefan Stoll and Arthur Schweiger. “EasySpin, a comprehensive software package for spectral simulation and analysis in EPR”. In: *Journal of Magnetic Resonance* 178.1 (2006), pages 42–55. ISSN: 1090-7807. DOI: <https://doi.org/10.1016/j.jmr.2005.08.013>. URL: <https://www.sciencedirect.com/science/article/pii/S1090780705002892> (cited on page 8).
- [TG96] Alberto Tannús and Michael Garwood. “Improved Performance of Frequency-Swept Pulses Using Offset-Independent Adiabaticity”. In: *Journal of Magnetic Resonance, Series A* 120.1 (1996), pages 133–137. ISSN: 1064-1858. DOI: <https://doi.org/10.1006/jmra.1996.0110>. URL: <https://www.sciencedirect.com/science/article/pii/S1064185896901102> (cited on page 28).
- [WSS92] Thomas Wacker, Gustavo A. Sierra, and Arthur Schweiger. “The Concept of FID-detected Hole-burning in Pulsed EPR Spectroscopy”. In: *Israel Journal of Chemistry* 32.2-3 (1992), pages 305–322. DOI: <https://doi.org/10.1002/ijch.199200038>. eprint: <https://onlinelibrary.wiley.com/doi/pdf/10.1002/ijch.199200038>. URL: <https://onlinelibrary.wiley.com/doi/abs/10.1002/ijch.199200038> (cited on page 39).
- [WJ18] Nino Wili and Gunnar Jeschke. “Chirp echo Fourier transform EPR-detected NMR”. In: *Journal of Magnetic Resonance* 289 (2018), pages 26–34. ISSN: 1090-7807. DOI: <https://doi.org/10.1016/j.jmr.2018.02.001>. URL: <https://www.sciencedirect.com/science/article/pii/S1090780718300466> (cited on page 42).
- [WS07] W. M. Witzel and S. Das Sarma. “Multiple-Pulse Coherence Enhancement of Solid State Spin Qubits”. In: *Phys. Rev. Lett.* 98 (7 Feb. 2007), page 077601. DOI: [10.1103/PhysRevLett.98.077601](https://doi.org/10.1103/PhysRevLett.98.077601). URL: <https://link.aps.org/doi/10.1103/PhysRevLett.98.077601> (cited on page 56).
- [ZJG05] Paul-Philipp Zänker, Gunnar Jeschke, and Daniella Goldfarb. “Distance measurements between paramagnetic centers and a planar object by matrix Mims electron nuclear double resonance”. In: *The Journal of Chemical Physics* 122.2 (2005), page 024515. DOI: [10.1063/1.1828435](https://doi.org/10.1063/1.1828435). eprint: <https://doi.org/10.1063/1.1828435>. URL: <https://doi.org/10.1063/1.1828435> (cited on page 40).





# Index

## A

adiabatic passage .....	26
adiabaticity .....	27
arbitrary waveform generator .....	24
average Hamiltonian theory .....	23
AWG .....	24

## B

Bloch-Siegert shift .....	23
---------------------------	----

## C

chirp waveform .....	25
----------------------	----

## D

DDS .....	24
deadtime .....	26
density operator .....	12

## F

fast passage .....	26
FID-detected hole burning .....	39
frequency sweep .....	24

## G

Gaussian pulses .....	29
-----------------------	----

## H

Haupt effect .....	19
high turning-angle pulse .....	41
high-temperature approximation .....	18
homogeneous broadening .....	38
hyperbolic secant pulses .....	28

## I

inhomogeneous line broadening .....	37
interaction frame .....	15

## L

linear regime .....	25
Liouville space .....	17
Liouvillian .....	17

## P

para-hydrogen induced polarization ....	19
Pauli matrices .....	12
PHIP .....	19
power broadening .....	38
pseudo-secular .....	40

## Q

quality factor .....	25
----------------------	----

**R**

- rotating frame ..... 22
- rotating-wave approximation ..... 22

**S**

- spectral diffusion ..... 38
- spin bath ..... 14
- spin operators ..... 11
- spin packet ..... 28
- stochastic Liouville equation ..... 17

**W**

- WURST pulses ..... 30